Article

Automating the Acoustic Detection and Characterization of Sea Ice and Surface Waves

Savannah J. Sandy [1,*], Seth L. Danielson [1] and Andrew R. Mahoney [2]

1   College of Fisheries and Ocean Sciences, University of Alaska Fairbanks, Fairbanks, AK 99775, USA
2   Geophysical Institute, University of Alaska Fairbanks, Fairbanks, AK 99775, USA
*   Correspondence: ssandy3@alaska.edu

Abstract: Monitoring the status of Arctic marine ecosystems is aided by multi-sensor oceanographic moorings that autonomously collect data year-round. In the northeast Chukchi Sea, an ASL Environmental Sciences Acoustic Zooplankton Fish Profiler (AZFP) collected data from the upper 30 m of the water column every 10–20 s from 2014 to 2020. We here describe the processing of the AZFP's 455 kHz acoustic backscatter return signal for the purpose of developing methods to assist in characterizing local sea ice conditions. By applying a self-organizing map (SOM) machine learning algorithm to 15-min ensembles of these data, we are able to accurately differentiate between the presence of open water and sea ice, and thereby characterize statistical properties surface wave height envelopes and ice draft. The ability to algorithmically identify small-scale features within the information-dense acoustic dataset enables efficient and rich characterizations of environmental conditions, such as frequency of sparse ice floes in otherwise open water and brief open-water leads amidst the ice pack. Corrections for instrument tilt, speed of sound, and water level allow us to resolve the sea surface reflection interface to within approximately 0.06 ± 0.09 m. By automating the acoustic data processing and alleviating labor- and time-intensive analyses, we extract additional information from the AZFP backscatter data, which is otherwise used for assessing fish and zooplankton densities and behaviors. Beyond applications to new datasets, the approach opens possibilities for the efficient extraction of new information from existing upward-looking sonar records that have been collected in recent decades.

Keywords: acoustics; upward-looking sonar; sea ice; waves; Chukchi Sea; Chukchi Ecosystem Observatory; mooring; Acoustic Zooplankton Fish Profiler; self-organizing map

1. Introduction

1.1. Overview and Rationale

The Arctic is undergoing rapid change [1], and continuous, year-round environmental measurements are needed to understand its seasonal and interannual variability and how these conditions support and structure the local ecosystem. Sea ice is a fundamental component of the Arctic marine system, influencing heat [2], freshwater [3], and radiative and turbulent heat fluxes between the atmosphere and the ocean [4] as it contributes to global climate regulation [5]. It provides an important habitat for species spanning all trophic levels [4,6], and residents of Arctic coastal communities depend on the sea ice for hunting and transportation to sustain their way of life [4]. As the Arctic continues to warm (e.g., [7]), monitoring sea ice conditions is needed to understand ongoing change and to better anticipate future marine conditions. In this paper, we describe an approach that improves our ability to characterize the sea ice environment using moored multi-purpose acoustic sensors.

Oceanographic research in polar regions entails special operational challenges; research efforts are expensive and logistically difficult, requiring ships and equipment capable

of working in remote, ice-covered conditions. The presence of sea ice in winter months especially impedes ship-based sampling, often resulting in a lack of in situ data through large portions of each year. Bias of existing data toward ice-free seasons thus hinders a more complete mechanistic understanding of the system. Due to sea ice formation, oceanic current flow patterns, and water mass transformations, the Arctic shelves seasonally experience significant physical and biogeochemical variability [8–10]. Long-term, year-round monitoring is used to build a more complete picture of the Arctic environment, the functioning of its marine ecosystem, and how they may be impacted by a changing climate.

1.2. Environmental Setting

An Arctic marginal sea, the Chukchi connects the Bering Sea and the greater North Pacific Ocean to the Arctic Ocean (see Figure 1). The Chukchi is a broad, shallow inflow shelf [11], extending approximately 500 km in the zonal direction and 800 km in the meridional direction with an average depth of about 50 m [8,12]. The nutrient-rich Anadyr Current feeds northward into the Chukchi through Bering Strait [13,14], making the Northern Bering and Chukchi seas some of the most productive marine systems in the world, with carbon fixation rates of up to 250–300 g C m^{-2} yr^{-1} [6,13–16]. Sea ice is commonly present on the Chukchi Sea shelf from approximately November to July, reaching a level (undeformed) ice thickness of ~1.5 m before seasonal melt is triggered by incoming solar radiation and heat transported north through Bering Strait [2,9,16–18].
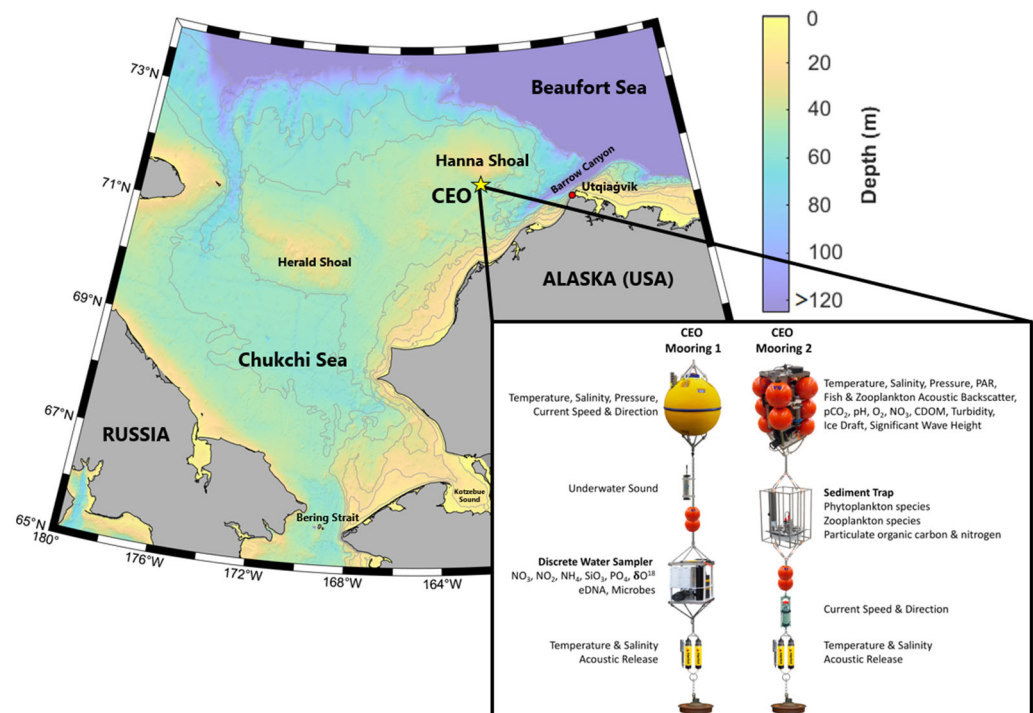

Figure 1. Map of the Chukchi Sea showing water depths. Bathymetric contours mark 100, 60, 50, 40, 30, 20, and 10 m depths. The CEO mooring site is marked with a yellow star, and the figure insert shows a diagram of the 2017–2018 CEO mooring configuration and measurement parameters. To measure acoustic backscatter, the Acoustic Zooplankton Fish Profiler (AZFP) instrument is located at the top of Mooring 2.

The oval-shaped Hanna Shoal (~162° W, 72° N; Figure 1) influences sea ice movement and thickness in the northeast (NE) Chukchi Sea. With a minimum depth of approximately 20 m, Hanna Shoal causes the grounding of deep ice keels, which in turn can lead to the regional persistence of sea ice into the summer [10,19]. The shoal's shallow topography steers the shelf flow field as it crosses the shelf en route to the Arctic Ocean. The southern flank of the shoal is believed to have weak current flow [10,20] and persistently cold bottom

water (−0.7 °C annual mean); the slow currents allow settlement of suspended particulate matter, feeding a benthic biological "hotspot" that sustains a walrus foraging ground [21] and provides a valuable food source for fish, seabirds, and other marine mammals including gray whales and bearded seals [20,22].

To meet the observational challenges outlined above, the Chukchi Ecosystem Observatory (CEO; http://chukchiecosystemobservatory.org/; accessed on 12 November 2020) was initially deployed in 2014 [23,24] as part of the North Pacific Research Board's (NPRB's) Long Term Monitoring program and in support of the build-out of the Alaska Ocean Observing System's (AOOS's) marine ecosystem implementation plan [25]. The CEO is a set of annually recovered and re-deployed subsurface moorings arrayed in the NE Chukchi Sea at 71.6° N and 161.5° W, located 110 km off of the Alaska coast between Hanna Shoal and Barrow Canyon (Figure 1). The CEO is generally comprised of two to three moorings per year carrying a suite of sensors: dataloggers for temperature, salinity, and ocean optics, passive and active acoustics, sediment traps [26], and biogeochemical sensors. An ASL Acoustic Zooplankton Fish Profiler (AZFP) on the CEO collects data from acoustic scattering sources including zooplankton, fishes, sea ice, frazil ice platelets, and the ocean surface. This versatility makes the AZFP well suited to the CEO's multidisciplinary mission. Although acoustic studies of sea ice draft are typically undertaken with upward-looking sonar (ULS) instruments dedicated to the task of ice detection (e.g., [27,28]), the AZFP is itself a ULS, although the AZFP ping rate (~20 s) is considerably slower than that of typical ULS instruments (~1 s ping rate). Despite the sample rate limitation, this study demonstrates that the AZFP can be used to investigate properties of the ocean surface and sea ice above the mooring and how these change on time scales of minutes to years.

1.3. Acoustic Detection of Sea Ice from Below

ULS instruments on oceanographic moorings collect temporally and vertically high-resolution data that can be used to describe the topography of the sea ice from below, and of the ocean–atmosphere interface when sea ice is not present. Deployed to remain below the reach of sea ice keels, a ULS can autonomously collect data all year long, regardless of weather and ice conditions. However, high-resolution acoustic data can be time-consuming and labor-intensive to process and analyze [27–29].

Determining ice draft involves the conversion of the travel time of a sonar acoustic pulse into an estimate of vertical distance between the ULS transducer and the underside of the sea ice. Using a moored pressure sensor, the local sea surface elevation is used as a reference for the calculation of sea ice draft, enabling corrections for fluctuations in speed of sound, and compensating for the lack of in situ information about water column structure above the instrument [30,31]. The reference sea level can be difficult to ascertain during periods of the year when it is obscured by ice cover for weeks or months at a time [27,28,31,32]. Determination of a reference sea level often requires manual analyses to identify open-water leads or polynyas that are then used to refine estimates of sound speed and sea ice draft.

The conditions of sea ice growth and decay affect the acoustic properties of ice [32–34]. As ice forms, ages, and ablates, it is subjected to processes that alter its physical characteristics including porosity, permeability, and roughness, which each have direct effects on acoustic scattering and attenuation [33]. Sea ice is especially sensitive to changes in temperature due to the inclusion of salts in the structure [33,34]. As the ice grows, brine pockets become increasingly constricted and isolated, reducing porosity and permeability. When sea ice begins to ablate in spring, brine channels grow and form tunneled connections with nearby pockets that eventually allow the brine to drain back into the ocean, influencing both the salinity of the water beneath the ice (which alters the speed of sound through the water column) and the ice's porosity [34]. When sensible heat is exchanged from the ocean to the ice, the under-ice surface is smoothed through the erosion of angular structures [33]. Such characteristics produce measurable differences in acoustic backscatter, and this information can be leveraged to distinguish open-water from ice-covered conditions,

and to characterize the sea ice environment as it changes throughout the year. Melling [32] demonstrated a difference in acoustic echo amplitudes between young and thin level ice, thick level ice, and ridge keels, showing that different sea ice types could be distinguished within ULS acoustic data.

Automating the detection of open-water segments in sea ice data has been attempted in numerous studies, with varying degrees of effectiveness. Algorithms automating the identification and tracking of leads have been developed using airborne [35] and satellite [36] imagery. Kvambekk and Vinje [30] outlined a method that analyzed ULS data in periods of 12–24 h in which the calculated draft statistics were subjected to certain thresholds and assumed to be open water if a number of predefined criteria were met. Strass [29] built upon this work and attempted an automated procedure that used short-term draft variability and echo amplitude variables to determine open water periods, but ultimately abandoned it for a more subjective system when it proved to be less effective during long intervals of little to no open water. Behrendt et al. [37] employed a system of identifying open water periods using the differences in the acoustic echo between water and ice and subjecting the results to an adjustable minimum threshold. Krishfield et al. [31] utilized a semiautomated approach by which sound speed was adjusted in three-hour segments using minimum draft thresholds when leads were present, and interpolating sound speed values through long periods of ice cover. Notably, a component of most of these methods is the need to manually define often subjective threshold values when determining open water from ice cover.

Modern computing power and analytical tools opens the door for efficient handling of increasingly large datasets. Our approach to the problem of differentiating sea ice from open water relies on the statistical power provided by aggregated ensembles of ice reflection statistics and the computational power provided by machine learning algorithms. This approach enables the detection of key patterns within large volume acoustic datasets without requiring predefined thresholds. It therefore represents a new level of automation in distinguishing open water from sea ice.

With the goal of developing a methodology that can more fully automate the processing of ULS data to facilitate subsequent environmental analyses, herein we analyze six years of subsurface mooring-based acoustic data collected from summer 2014 to fall 2020 in the NE Chukchi Sea. First, we outline a procedure to use the acoustic returns of an AZFP to calculate initial estimates of sea ice draft and wave height at the CEO site. Second, we separate periods of open water using a machine learning algorithm called the self-organizing map (SOM), and use these results to further refine the initial sea ice draft estimates. The resulting data can be applied to characterization of the local sea ice environment at the mooring site to gain a better understanding of seasonality, interannual variability, and acoustic nature of the ice over the mooring. We expect to detect interannual changes in the dates of ice onset and decay, in the density of sparse ice in summer and in the frequency of open water leads in winter. These characteristics represent potentially ecologically important changes to the physical habitat that supports the walrus, arctic cod, and other species that are endemic to the NE Chukchi Sea.

Section 2 details the processing and handling of the AZFP dataset, ancillary datasets from additional sensors co-located on the mooring cluster, and analysis techniques. Section 3 classifies ice-covered and open-water periods using the SOM algorithm and investigates the contrasting acoustic character of these two conditions. Sections 4 and 5 provide discussion and conclusions, respectively.

2. Materials and Methods

2.1. Data

The AZFP on the CEO is built by ASL Environmental Sciences of Sidney, BC, Canada, and is configured with four frequencies: 38, 125, 200, and 455 kHz. It sends acoustic pulses upward through the water column and records reflected echo amplitudes, which are subsequently scaled and adjusted for beam spreading to provide scattering volume (S_v)

in decibels relative to the transmitted signal. Our analyses are based on measurements of the 455 kHz transducer and a nominal speed of sound of 1450.5 m s^{-1}. The 455 kHz (7° beam width, which gives an open-water level surface footprint of approximately 12.8 m^2 over a distance of 33 m) return signal is digitized at a rate of 64 kHz and time-gated into discrete bins, giving a maximum achievable resolution of about 1.1 cm. The AZFP was deployed at depths of 28 m in 2014 and 33 m in all other years and programmed to ping at a rate of three to six times per minute (Table 1). In the second deployment year (2015–2016), six pings were averaged into 60-s ensembles onboard the instrument, while in the other deployments individual pings were recorded every 15 or 20 s.

Table 1. Details for each annual AZFP deployment, including the start time, target depth for the top of the CEO mooring frame, bin size, ping rate, and samples recorded. The CTD offset is an estimate of the distance between the pressure sensor and the AZFP transducer on the mooring.

Deployment Years	Start Date and Time (GMT)	Target Depth (m)	Bin Size (m)	Ping Interval (s)	Samples per Ping	CTD Offset (m)
2014–2015	20 September 2014 22:48:00	28	0.0113	15	3384	0.38
2015–2016	20 August 2015 16:53:00	33	0.0340	10	1176	0.84
2016–2017	4 August 2016 4:33:00	33	0.0113	20	3528	0.84
2017–2018	15 August 2017 1:03:00	33	0.0113	20	3528	0.84
2018–2019	6 August 2018 5:00:00	33	0.0340	15	1176	0.98
2019–2020	19 August 2019 16:03:00	33	0.0113	20	3529	0.84

To eliminate measurements taken during mooring placement and retrieval operations, one hour of AZFP data was removed from each end of all deployments. Echo returns from within 3 m of the transducer were also excluded from the dataset to eliminate nearfield acoustic ringing [38].

Measurements of temperature, salinity, and pressure were obtained from a Sea-Bird Scientific (Bellevue, WA, USA) SBE-16 SeaCat conductivity-temperature-depth (CTD) data-logger installed on the mooring adjacent to the AZFP (Figure 2). The CTD was calibrated at the manufacturer's factory prior to deployment in each year. Recovered data were screened for drift, spikes, and other possible error sources.

The CEO installation also includes a Teledyne RDI Waves Sentinel acoustic Doppler current profiler (ADCP) that is equipped with the functionality to measure significant wave height and direction. The ADCP recorded waves with a burst of pings every 1–4 h, depending on the deployment year. We use the ADCP-derived surface wave data, processed using the manufacturer's software, to assess the AZFP instrument's ability to generate estimates of surface wave height.

Atmospheric sea level pressure records were obtained from the European Centre for Medium-Range Weather Forecasts (ECMWF)'s ERA5 reanalysis (https://www.ecmwf.int/en/forecasts/dataset/ecmwf-reanalysis-v5; accessed 31 March 2021). The CTD and ERA5 datasets each have a time resolution of one measurement per hour. To associate environmental conditions with each ping, these datasets were linearly interpolated to the AZFP observation times.

True-color satellite imagery provided by NASA Worldview is used to compare cloud-free true-color remotely sensed sea ice conditions on mostly cloud-free days to the measurements made by the AZFP and the classifications made by the ice/open water delineation algorithm (https://worldview.earthdata.nasa.gov; accessed 4 February 2022).
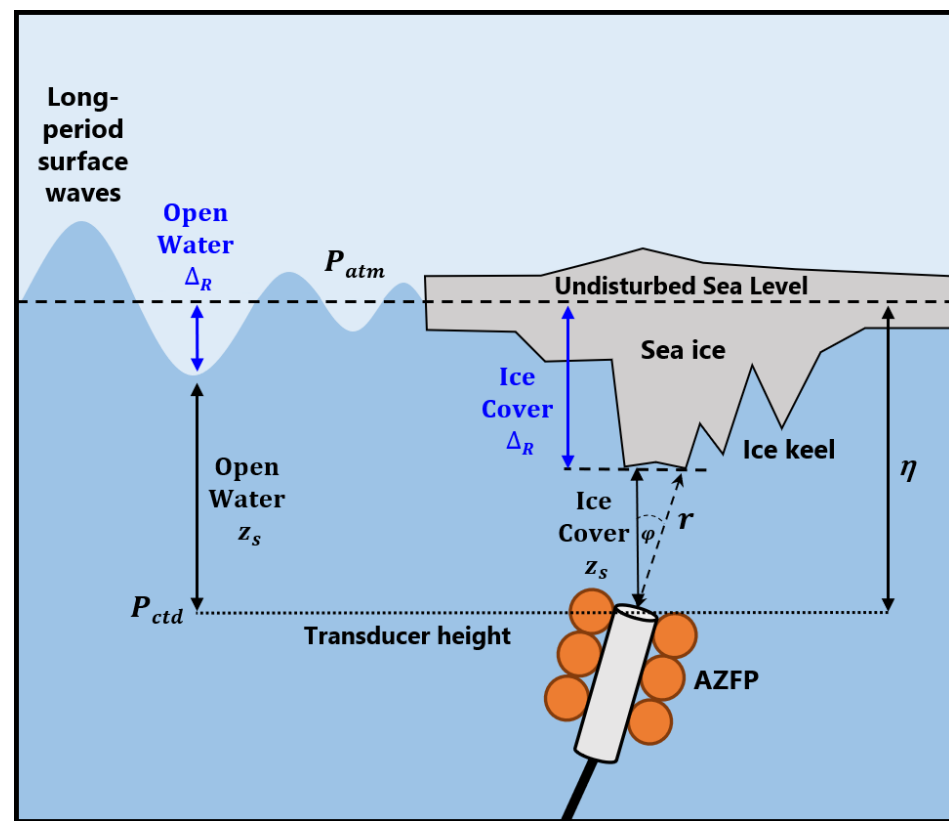
Figure 2. Diagram of the terms used to calculate Δ_R from AZFP data. Note that the long-period surface waves (e.g., tide waves, shelf waves) depicted in the figure do not include short-period surface capillary waves, wind waves, or swell.

2.2. Locating the Acoustic Reflection

For the general case of either ice-covered or open-water conditions, we form individual-ping estimates of the distance between the ocean surface, η, and the ocean–ice or ocean–atmosphere interface as:

$$\Delta_R = \eta - z_s. \tag{1}$$

Here, η is a reference sea level derived from the pressure measured by the moored CTD and reanalysis atmospheric sea level pressure, while z_s is the vertical (tilt-corrected) distance between the ice (or ocean–atmosphere interface) and the AZFP transducer. Tides storm surge waves, atmospheric pressure variations, and other low-frequency surface fluctuations that are resolved by the hourly CTD data are captured in both r (by the AZFP) and η (through the co-located CTD pressure sensor and the ERA5 estimates of the local atmospheric sea level pressure) terms. Such long-period waves are therefore removed from the Δ_R estimate by Equation (1). Hence, Δ_R estimates are calculated relative to a virtual (or nominal) reference plane that is best described as the undisturbed sea level, which is the sea level for which low-frequency surface fluctuations have been removed (i.e., fluctuations that are resolved by the CTD and ERA5 measurements. Wind waves, swell, and other short-period waves that are not resolved by the CTD pressure sensor represent a source of noise to any individual ping's ice draft estimate. Such short-period waves are high-frequency deviations from the undisturbed sea level. We note that many ULS instruments are equipped with a pressure sensor that is sampled at the time of each acoustic ping and for such datasets even many short-period waves can be removed from the Δ_R estimate. Our AZFP is not outfitted with a pressure sensor and thus we are forced to rely on the co-located but less frequently sampled CTD pressure record. We show below that when averaged over a 15-min ensemble, short period wave noise represents an acceptable magnitude of error in the final ice draft estimates.

To calculate z_s, we apply the formula:

$$z_s = \beta \cdot r \cdot cos(\varphi) \tag{2}$$

where r is the time-gated range between the AZFP transducer and the target of interest (either the sea surface or the bottom of the ice), φ is a correction for instrument tilt, and β is a correction for the speed of sound (Figure 2; [27]).

An initial estimate of instantaneous distance, r, from the AZFP transducer to the ice/ocean or ocean/atmosphere interface is obtained through analysis of individual ping echo amplitude profiles and amplitude gradient profiles. Acoustic returns during ice-free days and ice-covered days exhibit prominent peaks in the backscatter amplitude, which we take to represent the location of the acoustically reflecting surface (Figure 3). Comparison of the time-gated bin of maximum S_v amplitude to the bin of maximum S_v gradient magnitude shows the two to be identical 99.993% of the time across the six-year dataset, suggesting that the two methods are equally useful for identifying the reflection surface location. For the purpose of this study, we define the raw (uncorrected) distance from the AZFP transducer to the target as the bin of the maximum amplitude return signal.

The AZFP is subject to movement from forces acted upon the mooring by ambient currents. This movement causes slight instrument tilt, which affects the orientation of the transducer and the distance between the transducer and the ice directly above. To correct for transducer tilt, the AZFP records pitch, γ, and roll, α, in degrees. We apply a correction for instrument tilt, φ, according to the trigonometric relation:

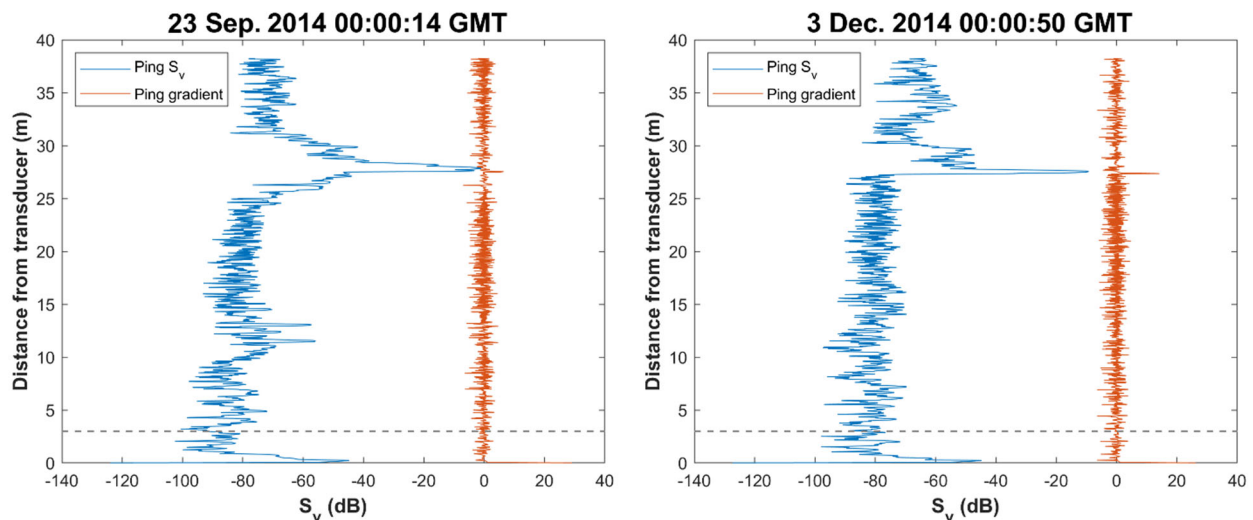$$\varphi = tan^{-1} \sqrt{tan^2(\alpha) + tan^2(\gamma)} \tag{3}$$

Figure 3. Representative acoustic return ping profiles from the AZFP dataset in open water (**left**) and ice cover (**right**). Each plot shows the acoustic backscatter amplitude scattering volume S_v of a single ping plotted over uncorrected distance from the AZFP transducer (blue), and the S_v gradient (red). The gray dashed line represents the 3-m nearfield echo exclusion zone.

The variable β in Equation (2) represents a correction factor for the sound speed variations in the water column. Seasonal variations in temperature and salinity exert non-negligible effects on density and thus the apparent distance from the AZFP transducer to the surface [27,28]. The correction is computed as a ratio between the true sound speed and our nominal sound speed of 1450.5 m s^{-1}. We applied an initial correction for the values of temperature, salinity, and pressure measured by the CTD at the AZFP depth, though some uncertainty remains due to a lack of information on the overlying water column; frequent CTD casts at the CEO site are logistically impractical. We can assess the potential error

induced by incomplete knowledge of the hydrographic structure by comparing speed of sound variations associated with maximum expected temperature and salinity variations. Given the efficiency of ice keels to induce mixing [39] and convective overturn associated with brine rejection as salts from forming sea ice are released into the ocean, [3], we assume a weakly stratified water column during late fall, winter, and early spring at this shallow shelf setting. At these times of year, we anticipate that 0–30 m depth temperature and salinity differences are typically less than 0.2 in °C and PSU (see, for example, Figure 4 of Hauri et al. [24]). Speed of sound uncertainty at a typical winter temperature of $-1.8\,°C$ and salinity of 32 PSU are less than 0.1% (sound velocity = 1437.1 m s^{-1} for T = $-1.8\,°C$ and S = 32 PSU; sound velocity = 1438.3 m s^{-1} for T = $-1.6\,°C$ and S = 32.2 PSU). With a two-way travel distance of 66 m for thin ice, such uncertainty would induce a z_s error of about 0.027 m; for a 10 m ice keel the uncertainty would be about 0.018 m. Since Δ_R decreases as z_s increases, the resulting uncertainty in ice draft is greater for thin ice than for thick ice.
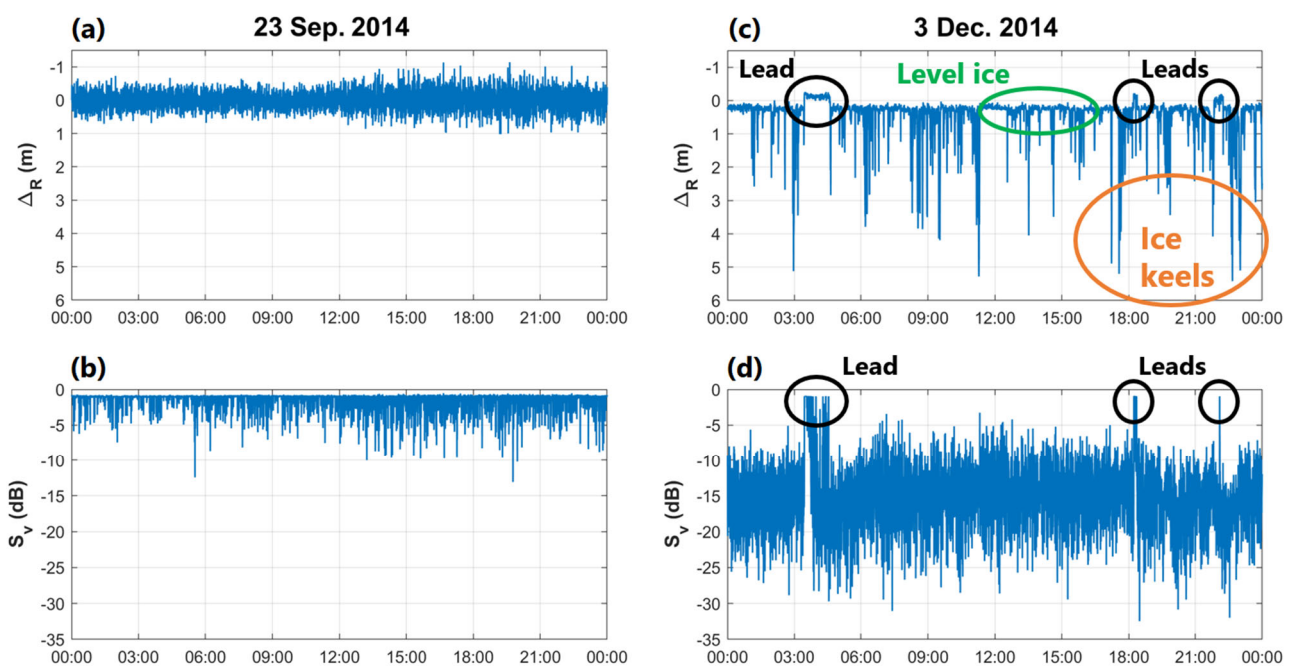

Figure 4. Δ_R (m, top panels) and S_v (dB, bottom panels) plotted for representative open-water (left) and ice-covered (right) 24-h intervals, respectively. 23 September (panels (**a**,**b**)), represents open-water conditions at the CEO site in the NE Chukchi Sea, and 3 December (panels (**c**,**d**)), represents ice-covered conditions. Highlighted features within the sea ice cover include: leads (circled in black), level ice (circled in green), and ice keels (circled in orange).

Deviations from the true speed of sound can be at least partially mitigated by incorporating our knowledge of β from the ice-free intervals. Common practice [27] is to use open-water events (e.g., leads and polynyas) that pass over the mooring to compute range corrections. To estimate β for the periods when ice is over the mooring, we compute the daily mean β for ice-free intervals of each day that contains more than 15 min' worth of open-water pings, and then linearly interpolate β in time between successive open-water tie points [27,28,37]. Changes in β over the course of one day are generally expected to be small. When ice is present, however, the undisturbed sea level may be obscured for weeks or even months at a time, during which uncertainty in sound speed corrections grows [28]—although this often occurs at a time of year when water temperature and salinity variations are relatively small. Calculation of β can be a labor-intensive process when identifying and selecting open-water events by hand [27,28].

The local reference surface elevation, η, is derived from the hydrostatic equation:

$$\eta = \frac{(P_{ctd} - P_{atm})}{\rho \cdot g} + \eta_A \tag{4}$$

where ρ is density calculated from the co-located CTD measurements of temperature, salinity, and pressure (T_{ctd}, S_{ctd}, P_{ctd}), respectively; P_{atm} is atmospheric pressure from ERA5; g is gravitational acceleration (9.8 m s^{-2}), and η_A is an alignment correction for zeroing the reference level, based on the open-water time intervals. P_{ctd} includes a correction for the location offset between the transducer and the CTD pressure sensor (Table 1). Recognizing that the calibrated CTD pressure measurement includes hydrostatic pressure of the water column referenced to zero at the bottom of the atmosphere, the appropriate atmospheric pressure correction P_{atm} is the deviation of atmospheric pressure from the local mean

$$P_{atm} = P_{ERA5} - mean(P_{ERA5}). \tag{5}$$

The local mean atmospheric pressure at the CEO site is approximately 1015 mbar (depending on year), so the calibrated CTD pressure reference of 14.7 psia (1013.53 mbar) represents an average offset of ~1.5 cm in height. This offset is accounted for in the final elevation correction. Harmonic analysis of the CTD pressure sensor (following Pawlowicz et al. [40]) shows that the magnitude of the resolved (signal-to-noise ratio > 2) tidal constituents sum to 16.8 cm, representing 14.7% of the total sea level variability at the CEO site.

An additional final adjustment, η_A, was applied to the entire dataset to bring it into alignment with the empirically identified reference mean sea level. This nearly negligible offset was determined by computing the mean Δ_R of all open-water pings across the 6-year dataset and applying this offset to the entire time series. For this dataset, $\eta_A = 0.002$ m.

Certain unquantifiable errors in Δ_R estimates and β exist in the form of: inaccuracies in Δ_R due to interactions of the sonar beam with target features in an off-axis position, uncertainties of the temperature and salinity profiles for the water column above the mooring, and potential errors introduced in the speed of sound correction due to lack of mid-winter open-water calibration tie points. Estimates of Δ_R are made with the assumption that the ULS target is on the axis of the sonar beam, when in practice the acoustic pulse areal footprint encounters ice features or waves in an off-axis position, causing a biased estimate of draft for that ping [28].

Additional errors may also be introduced by our method in using open-water periods to refine the speed of sound correction. When waves break, air bubbles are injected into the water column, sometimes to a depth of several meters or more. Since bubbles strongly scatter sound, studies found identification of the sea surface interface in heavily agitated water to be inaccurate and therefore unsuitable for use in speed of sound corrections [28,32]. Since our automated method utilizes all available open-water data, inaccuracies in the β calculation are expected to be largest during periods of storms and high winds. However, because we make daily estimates of β that are based on over 4000 pings per day, occasional pings that are biased due to bubbles have inconsequential impact on our β estimates. During periods of ice cover, there are fewer pings per day available for β estimations, but the presence of ice dampens surface waves and so we do not generally expect bubble injection from large breaking waves to coincide with the presence of ice cover.

To improve our accuracy in separating the presence of open water from sea ice, the full-resolution AZFP datasets are assembled into 15-min ensembles, and a suite of statistical metrics computed on each of the of Δ_R and S_v parameters. In addition to the ensemble arithmetic mean, we also evaluate each interval's standard deviation, minimum, maximum, range, skewness, and kurtosis.

2.3. Self-Organizing Map

As previously noted, deriving sea ice draft from acoustic data can be a labor-intensive process, in part because of the need to identify sometimes sparse open-water intervals that

provide a sea level reference [27,28]. To aid in distinguishing open water from ice cover, we turn to a self-organizing map (SOM) algorithm, a tool designed to extract characteristic patterns from large-volume and potentially noisy data (e.g., [41–43]). The SOM's utility makes it suitable for applications in a wide range of disciplines, including meteorology, biological and physical oceanography, agriculture, and economics [43,44]. A useful feature of the SOM framework is that it does not require any prior knowledge of the input datastream, meaning that it can function without the use of predefined or subjectively determined selection thresholds [42].

The SOM is based on an unsupervised neural network [43,45], and its resulting output allows for the simple visualization of otherwise complex or high-dimensional data. Through a recursive regression process, the SOM converts nonlinear statistical relationships between data into a low-dimensional gridded "map" from which relational patterns may be identified.

A MATLAB-based SOM Toolbox (http://www.cis.hut.fi/projects/somtoolbox/; accessed on 15 September 2021) drives the machine-learning signal analysis component of our study. The toolbox implements the SOM algorithm by accepting a data array containing an arbitrary set of input variables and subjecting it to one of three training algorithms (sequential, batch, or sompak) to identify a user-specified number of patterns. To start the sequential training process, each unit on the map is assigned a random weight. Input data from the high-dimensional space are passed into the SOM algorithm, which calculates the activation function (usually the Euclidian distance between the weight vector of the unit and the data). The weight vector of the unit with the highest activation (i.e., the smallest Euclidian distance) is termed the best matching unit (BMU), and the weight vector of the BMU is adjusted toward the input data. Additionally, a neighborhood function is applied to modify the weight vectors of adjoining units. This machine learning training phase then repeats until the map evolves into a steady solution. The result is a map in which similar data points are grouped more densely on the grid than unlike data points [41,43].

The batch and sompak training algorithms are similar, wherein all input vectors are simultaneously used to update all weight vectors. This method results in a training sequence that is faster and more computationally efficient than the sequential training process [43]. We process our data in this study using the batch training algorithm, and configure the training phase to run for ten iterations.

The SOM Toolbox has four available types of neighborhood functions: "gaussian," "cutgauss," "ep" (Epanechikov function), and "bubble." We tested all four and found no meaningful difference between results of three in accurately identifying open-water segments. The fourth, the bubble function, designated all ensembles as open water and therefore is not a valid choice for this application. For this study, we utilize the ep function. For more information about the SOM Toolbox, including the equations used in the activation and neighborhood functions and a performance evaluation, see Liu et al. ([43]).

Assuming a priori (justifications provided in Section 3 and by the studies referenced in Section 1.1) that ice-ocean and ocean–atmosphere interfaces exhibit contrasting acoustic characteristics, we configure the SOM algorithm to search for two patterns in the 15-min AZFP statistics listed in Section 2.2. The BMUs thus provide a separation of the data at 15-min intervals that are associated with primarily either open water or sea ice present above the CEO mooring. As the SOM can be sensitive to signal variance, we normalized each variable by subtracting its mean and dividing this by the record length standard deviation. We subject the SOM results to sensitivity testing to identify the optimal input parameters, averaging period, and input variables to use for the identification of open water and ice cover.

Application of the SOM algorithm is presented in Section 3.3.

2.4. Automating the Construction of Δ_R

Combining the signal handling and analysis techniques described above, we can construct an automated procedure applicable to generic ULS datasets. Such an algorithm

(Figure 5) is based on Equation (1) to calculate Δ_R and the SOM neural network. With notable fidelity, the SOM identifies open-water intervals within otherwise extensive sea ice cover, and sparse ice in periods of primarily open water.
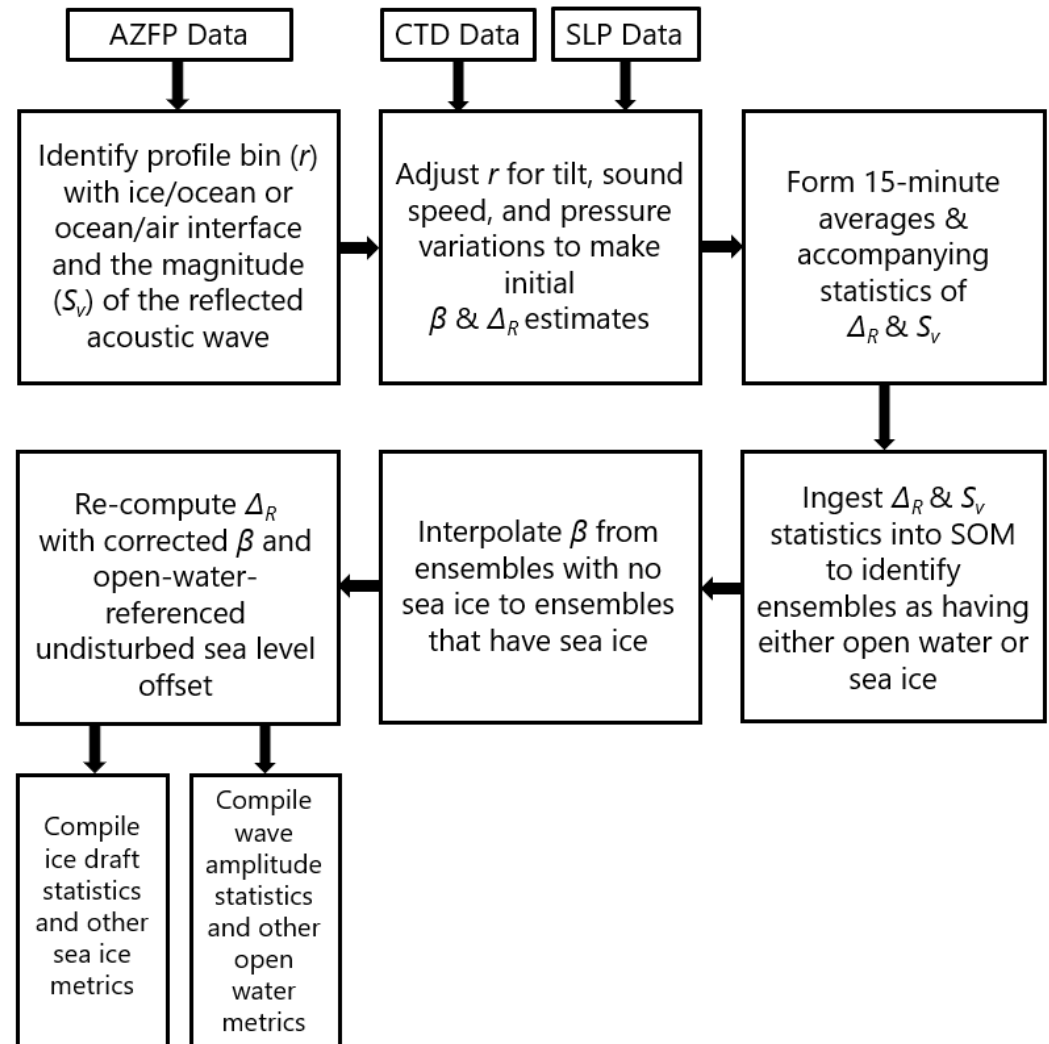

Figure 5. Signal processing flow chart detailing steps for automating estimates of sea ice draft, wave amplitude, and associated statistics from the upward-looking sonar Acoustic Zooplankton Fish Profiler (AZFP) acoustic backscatter data and accompanying conductivity-temperature-depth (CTD) and atmospheric sea level pressure (SLP) datasets. S_v represents the amplitude of the acoustic backscatter relative to the transmitted signal, r is the raw (unadjusted) distance from the acoustic transducer to the ice/ocean or ocean/atmosphere interface, β represents a correction for changes in the speed of sound due to water density fluctuations, and Δ_R is the calculated difference between the mean sea level and the sea surface/bottom of the ice. A self-organizing map (SOM) machine learning algorithm identifies intervals of open water and sea ice cover.

From the individual AZFP pings we first extract the bin containing the maximum echo return amplitude (S_v), and use this to estimate the distance from the AZFP transducer to the ocean–atmosphere or ocean–ice interface. AZFP pitch and roll measurements correct the acoustic range estimate for instrument tilt, and CTD and atmospheric sea level pressure data enable initial sound speed and surface wave corrections, providing a surface reference for initial ice draft estimates (Δ_R). Lacking data about stratification of the water column above the mooring, we use open-water periods to compute the β correction and take these elements into account.

To identify open-water periods in the midst of sea ice over the CEO site, we begin by combining the AZFP Δ_R and S_v datasets into 15-min ensembles and computing statistical summaries for each ensemble. These metrics provide the input variables for the SOM algorithm, which assigns variables to one of two modes, representing open water and ice cover. We use the ensembles that are identified as Mode 1 (open water) as year-round surface calibration tie points, interpolating β values between the tie points and onto the ensembles identified as Mode 2 (sea ice). The open-water calibration tie points are identified using the SOM algorithm Thereafter, we are able to re-compute final Δ_R estimates that represent ice draft.

To assess the benefit of the β correction, we compute the mean and standard deviation of the 15-min ensemble Δ_R estimates from prior to the final β correction, obtaining a level sea surface estimate having a Δ_R root-mean-square error of 0.30 m and a standard deviation of 0.20 m, calculated across all open-water ensembles. After the final β correction, those values decrease to ~0.06 m and 0.09 m, respectively, demonstrating the effectiveness of using the SOM-identified open-water ensembles to refine the β correction. From the final estimates of Δ_R and the SOM Mode 1/Mode 2 separations, we can compile metrics and statistics for sea ice draft and wave amplitudes, depending on research needs.

3. Results

3.1. Acoustic Reflection Characteristics

To demonstrate acoustic differences between open water and ice cover, we select one 24-h interval in the pre-freeze-up (open water) season of 2014 (23 September) and one 24-h interval post-freeze-up (3 December). According to passive microwave satellite measurements from the National Snow and Ice Data Center [46,47], 23 September is reported as having a 0% ice concentration over the CEO site, with at least two more ice-free days before and after that date. December 3rd likewise was reported to have 100% sea ice concentration, within a cluster of other 100% ice-covered days. Inspection of the AZFP dataset reveals that the acoustic properties of 23 September and 3 December are well representative of typical open-water and ice-covered days, respectively.

The Δ_R and S_v estimates for all pings within each of the selected 24-h periods show measurable differences between open-water and ice-covered conditions (Figure 4). While the ice-cover signal shows a greater range in Δ_R excursions due to ice keels, the open-water signal contains the effects of larger-amplitude surface waves and swell during ice-free conditions. The Δ_R values of the open-water day are generally symmetrical around zero (i.e., the undisturbed sea level), while the ice-cover values are skewed downward into the water column due to the presence of sea ice and ice keels. The measurements of S_v also exhibit a difference between the two days, with backscatter amplitude much greater for the open-water conditions than for sea ice cover. Figure 4d also shows three periods of time (just after 03:00, 18:00, and 21:00 GMT) where Δ_R is close to 0 m and which appear to be leads within the ice cover (i.e., brief periods of open water or very thin ice). These leads are associated with S_v measurements that are close to 0 dB, and similar in magnitude to the open-water day reflection amplitudes. Together, these observations show that the ocean–ice interface has a measurably different acoustic character than the ocean–atmosphere interface, a finding that is consistent with prior investigations (e.g., [32,33,48]).

We expect that variations in sea ice roughness, porosity, and permeability all have effects on how acoustic waves are scattered, reflected, or attenuated, and that are exhibited in the measured S_v returns from the AZFP. Color-shading Δ_R as a function of S_v for the entire six-year AZFP dataset (Figure 6) shows a transition between periods of open water and periods of ice cover. During the months between summer break-up and winter freeze-up, the acoustic backscatter amplitude recorded by the AZFP is greater than the backscatter amplitude recorded during the winter ice-covered months. However, one can also detect instances of high-amplitude "summer" type reflections in the presence of thick ice keels in spring.
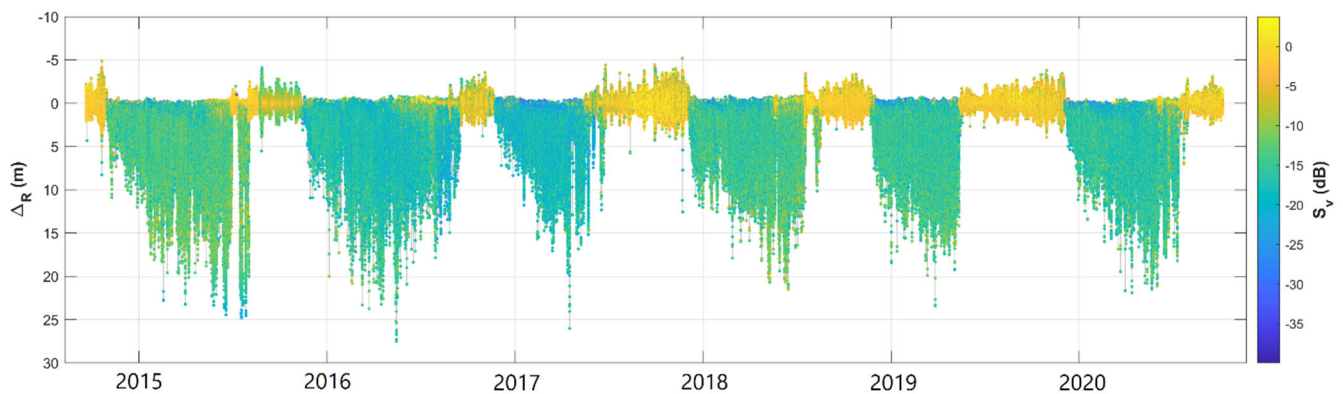
Figure 6. Δ_R (m) time series for the full-resolution six-year AZFP dataset at the CEO site in the NE Chukchi Sea, color-shaded by S_v (dB).

The visualization of echo amplitude (Figure 6) reveals details about the character of the seasonal cycles at the CEO site. For example, the open-water seasons in 2017 and 2019 appear to be longer (by a month or more) than that of the other deployment years. Temperature records (not shown) from the CTD onboard the CEO moorings at approximately the same depth as the AZFP show that the water temperatures for 2017 and 2019 were higher than any other year in the AZFP record, with temperature maximums reaching just over 4 °C in October and November, respectively. In contrast, the highest temperature recorded in the autumn of 2018 was approximately 1.6 °C. Such differences in water temperature may be influenced by variability in heat transported north through Bering Strait and air–sea heat exchanges local to the Chukchi Sea [2,7].

3.2. Statistics of the Return Echoes

While Δ_R and S_v provide contrasting information in the presence of sea ice and open water, examination of the data reveals that these metrics alone are not fully sufficient for differentiating the two conditions. Wind acting upon open water causes the ocean–atmosphere interface to vary in range, often by several meters during summer storms (Figure 6). The initial formation of sea ice can be difficult to identify when ice is not thick enough to be distinguished from the background noise of wind waves. Thus, we turn to the 15-min statistics (Section 2.2) to provide additional metrics that can be more robustly delineate ice cover from open water.

All of the selected statistics for both Δ_R and S_v (Figure 7 shows the 2014–2015 deployment as an example) exhibit transitions from open water to ice cover (in 2014, late October) and a return to open-water conditions (in 2015, late June, with brief periods of ice cover during the latter half of July and early August). Periods of open water generally exhibit Δ_R and S_v values closer to zero than periods of ice cover. Skewness and kurtosis of S_v values are closer to zero during winter months. In the Δ_R minimum statistic, the seasonal transition is marked by a shift from negative values to positive values. The transition from open water to sea ice in late October is visible in nearly all plots of Figure 7; however, notable in the plots of S_v for this deployment (Figure 7b) is an extended transition to open water that begins in mid-May, where the acoustic character of the signal changes long before break-up becomes apparent in measurements of Δ_R (Figure 7a). Each of the metrics exhibits an identifiable difference between the ice-covered periods and the open-water periods, indicating that they are all potentially useful in classifying ice conditions over the mooring.

In Figure 8, kurtosis is plotted against skewness of both Δ_R and S_v for the open-water and ice-covered example days shown in Figure 3. In general, the kurtosis and skewness of the open-water conditions are lower than that of the ice-covered conditions for Δ_R, with a lower variance for the open-water values. Likewise, the skewness of the S_v for the open-water day is also lower than that of the ice-covered day, but the open-water day has a higher kurtosis and variance. Panels in Figure 8a,b show an apparent delineation between the

open-water day and the ice-covered day. The delineation becomes more distinct when the pings of the open-water and ice-covered days are averaged into hourly ensembles (panels in Figure 8c,d). The 15-min ensembles exhibit some overlap, indicating that skewness and kurtosis cannot be relied on solely to determine if a 15-min period is most likely to be open water or ice-covered, but nevertheless the relationship between the two variables highlights their usefulness for this application.
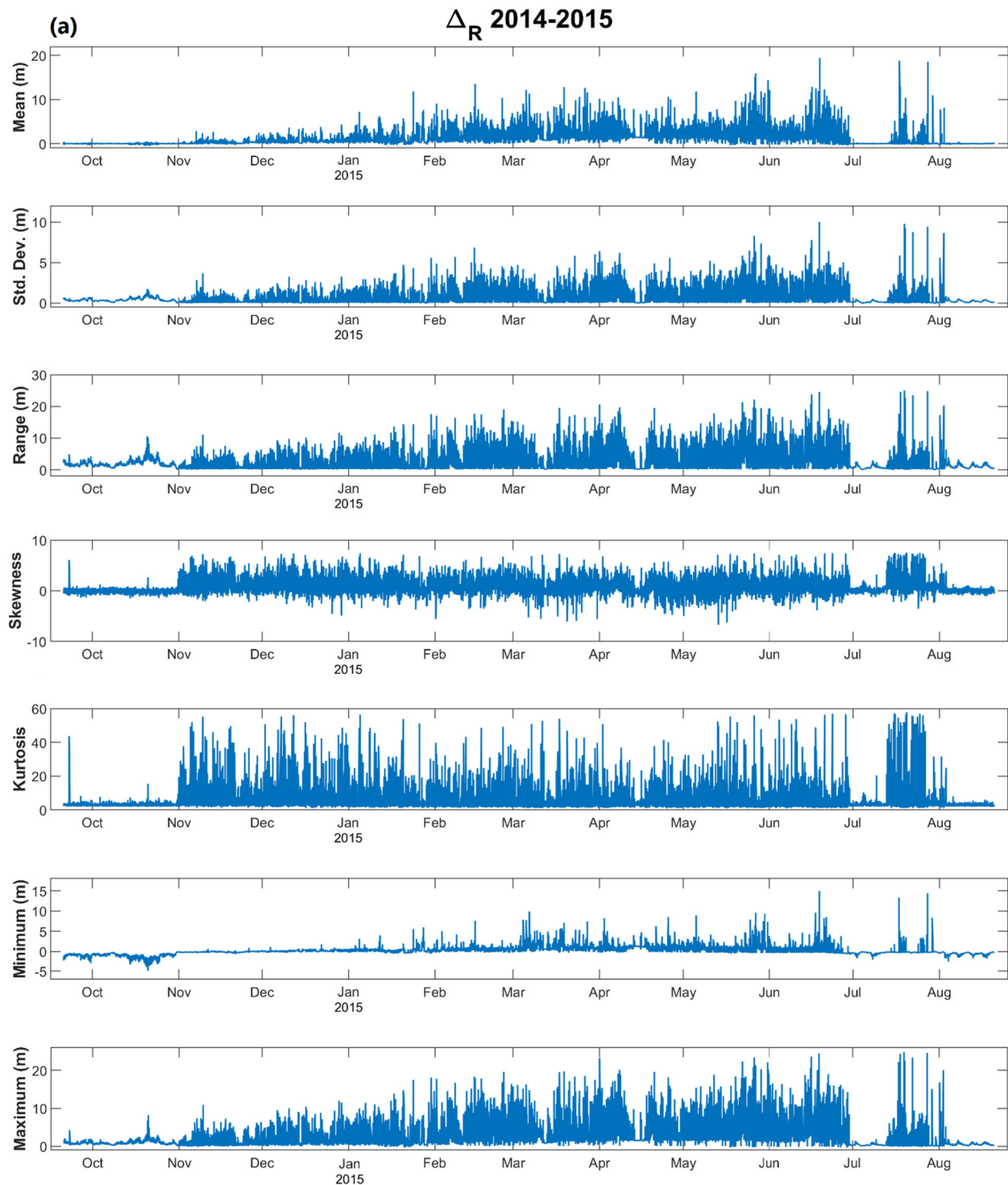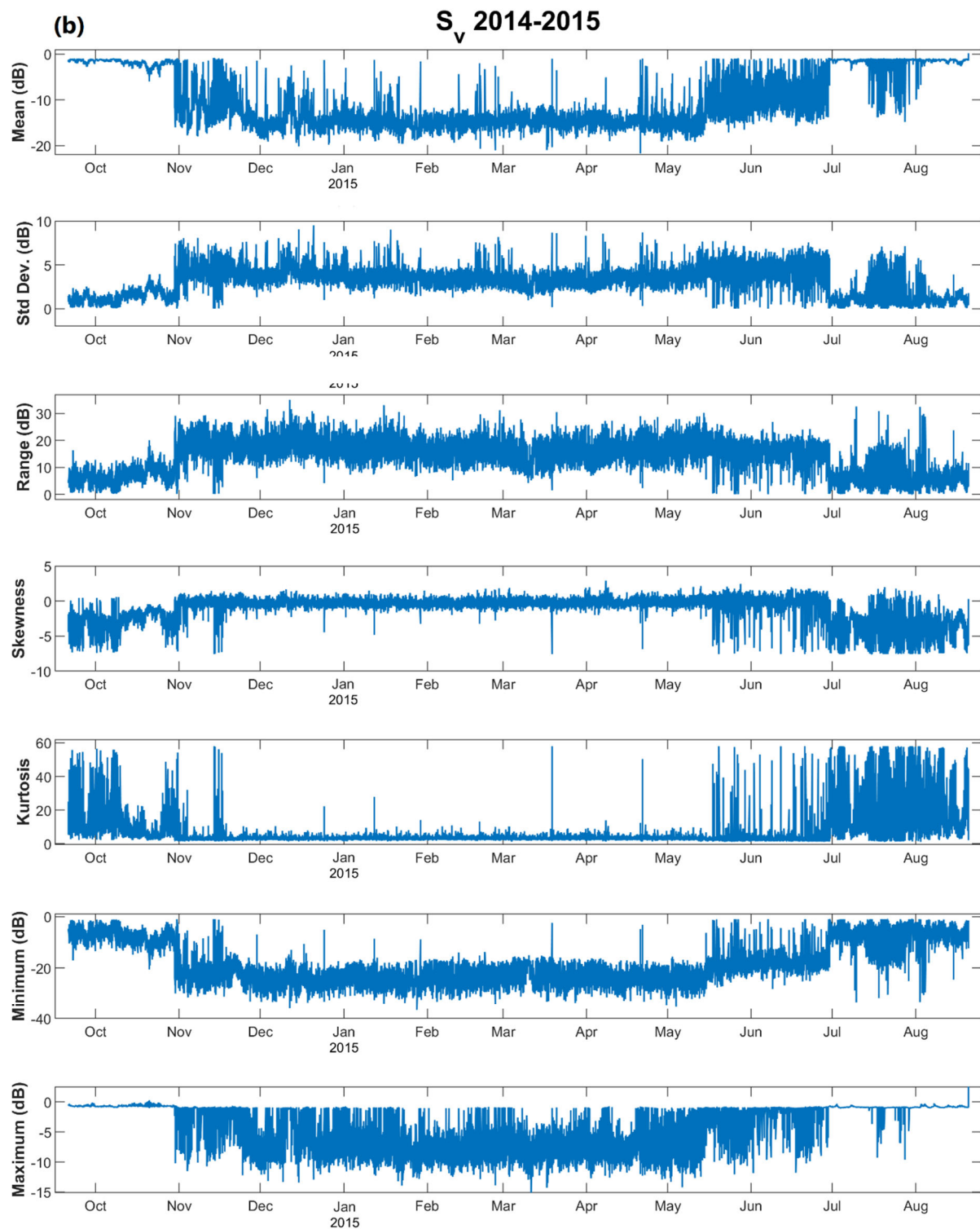

Figure 7. *Cont.*

Figure 7. Time series of statistics for Δ_R and S_v for the 2014–2015 AZFP deployment in the NE Chukchi Sea, computed on the 15-min ensembles. From top panel to bottom panel, parameters shown are: mean, standard deviation, range, skewness, kurtosis, minimum, and maximum for both Δ_R (**a**) and S_v (**b**). With many instances of leads and otherwise shifting ice conditions, the mooring was mostly covered by sea ice from approximately 1 November 2015 to 30 June 2016 and 13 July 2016 to 3 August 2016.
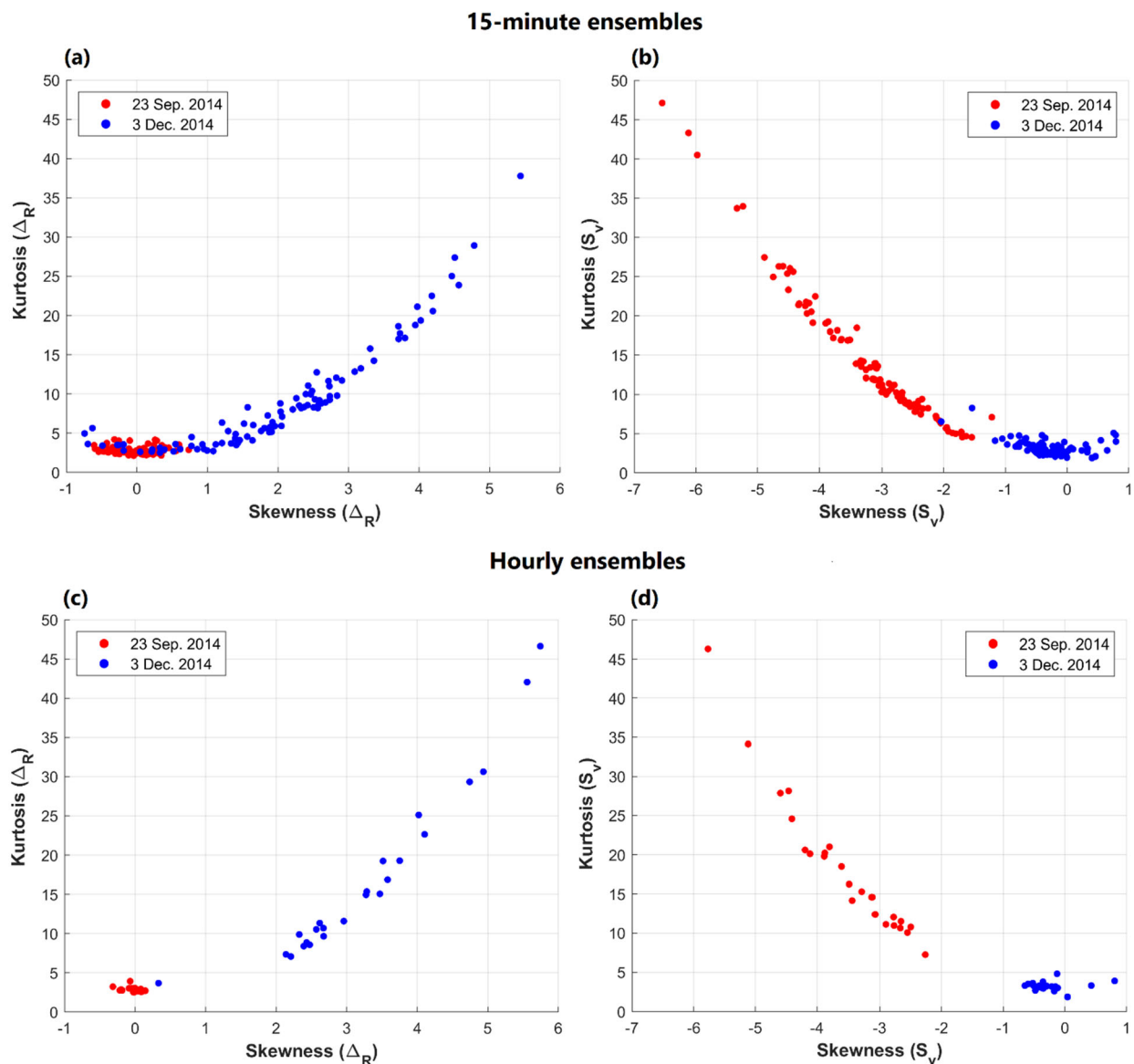
Figure 8. Kurtosis plotted against skewness for representative Acoustic Zooplankton Fish Profiler (AZFP) data over 24 h of open water (red; 23 September 2014) and ice-covered (blue; 3 December 2014) conditions. Statistics are computed over 15-min (upper panels (**a**,**b**)) and hourly (lower panels (**c**,**d**)) ensembles at the CEO site in the NE Chukchi Sea. Kurtosis and skewness are calculated for both Δ_R (left panels (**a**,**c**)) and S_v (right panels (**b**,**d**)).

3.3. Delineating Sea Ice and Open Water with SOM Analysis

As noted above, Δ_R, S_v, and the statistical metrics such as skewness and kurtosis are each individually insufficient for delineating periods of open water and sea ice, so we provide our time-averaged data and statistic al metrics to the SOM algorithm. We configured the SOM to search for two patterns in the AZFP data, which we will demonstrate are representative of open water (Mode 1) and ice cover (Mode 2). Results of the SOM analysis based on all 14 input variables (listed in Section 2.2) suggest that the algorithm exhibits appreciable skill in delineating the presence of sea ice and open water (Figures 9–13).
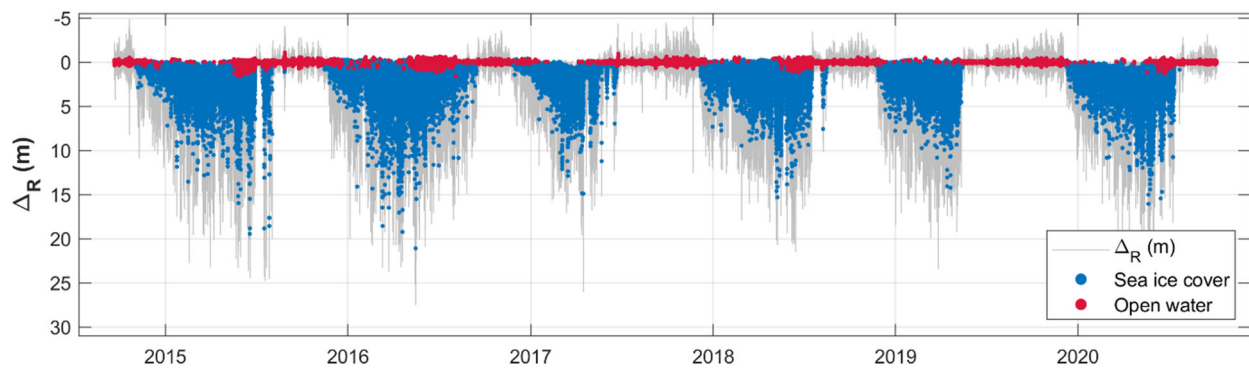
Figure 9. Plot of Δ_R with the SOM analysis. The full-resolution time series of Δ_R from the AZFP in the NE Chukchi Sea is plotted in gray, with each 15-min period Δ_R mean marked as Mode 1 (open water; red) or Mode 2 (ice cover; blue) according to the SOM. Note the existence of many open water ensembles in the presence of ice cover, representing sound speed correction tie points.

We test four AZFP averaging intervals for statistical and SOM analyses: 10, 15, 30, and 60 min. All periods produce similar estimates of ice cover: for the 2014–2015 deployment, the 10-min period SOM identifies 72.3% of ensembles as Mode 2, a 15-min period 71.3%, a 30-min period 73.3%, and a 60-min period 72.8%. While the small number of ensembles that differ depending on the ensemble selected appear throughout the record, the majority of them are concentrated in the transition periods from open water to ice cover and back again. Smaller ensemble intervals tend to be associated with disagreements later after freeze-up and earlier before break-up (a difference of several days in the 2014–2015 deployment). Such differences could potentially impact estimates of freeze-up and break-up dates).

The SOM Toolbox also supplies a metric of map quality denoted the quantization error (QE), defined as the mean distance between each data point and the BMU [43]. In general, a lower QE indicates a map that better matches the data. The QE is the lowest for the 60-min period (2.52) and increases incrementally as the time periods shorten (the 30-min period's QE is 2.54, the 15-min period's is 2.56, and the 10-min period's is 2.58). However, the 30- and 60-min periods do not delineate clear but short duration instances of ice cover and open water that are captured in the 10- and 15-min ensembles. We therefore use the 15-min period in this study in order to balance temporal precision and SOM QE, maximizing the number of pings in each ensemble for improved statistics (e.g., 50% increase in the number of pings per ensemble from 10-min to 15-min ensembles and a corresponding decrease in 95% confidence limits).

We also test whether the SOM results are sensitive to any individual variable by running the SOM algorithm through a series of 14 iterations, removing one variable each time. We find that in comparing the result to the SOM run with all variables included, no single variable accounts for more than a 1.3% difference in mode identification by its removal, suggesting that none of the variables has a disproportionately large influence on the outcome of the SOM by itself. Conversely, in running the SOM algorithm on each variable individually, we find a minimum of 23% difference in mode identification, reinforcing the idea that the best approach for using the SOM to detect open water involves a combination of variables.

In order to test the relative magnitude of importance each variable has on the SOM, and thus whether certain variables are more useful in this context than others, we also run an iterative stepwise test by which the "best" single variable (i.e., the variable that produces a map with the fewest differences from the map resulting from the use of all 14 variables) is selected. We then run this dataset through the SOM algorithm in combination with each of the remaining variables. The best combination from that iteration is then selected and run in turn with each remaining variable, etc. until no variables remain. This test shows that three variables (mean S_v, range of S_v, and minimum of Δ_R) produce a BMU map that is in 98.6% agreement with the map that includes all 14 variables. While this

result suggests that a subset of all variables may be used to produce a map of meaningful accuracy, depending on the application, some caution must be taken in deciding which variables to exclude. For example, while the SOM for the 15-min period averaging indicates that the mean S_v is the third highest variable in terms of influence on the map, it is only the twelfth highest variable for the SOM in which 60-min averaging was employed. For the purpose of this study and because computational power is not a limiting factor for this number and length of input fields, we use all 14 variables to maintain the highest possible accuracy in identification of the open water and ice cover modes.

A visual inspection of the SOM output for the AZFP data shows that the algorithm appears to be quite skillful in separating open water from sea ice cover. An example from 7 August 2016 (Figure 10), provides an example of mostly open water but with ice keels up to ~12 m depth occasionally passing over the mooring. In this example, which is well representative of any randomly selected time interval, the algorithm appears to correctly identify the vast majority of unambiguous instances of sea ice and open water based on analyst interpretation.
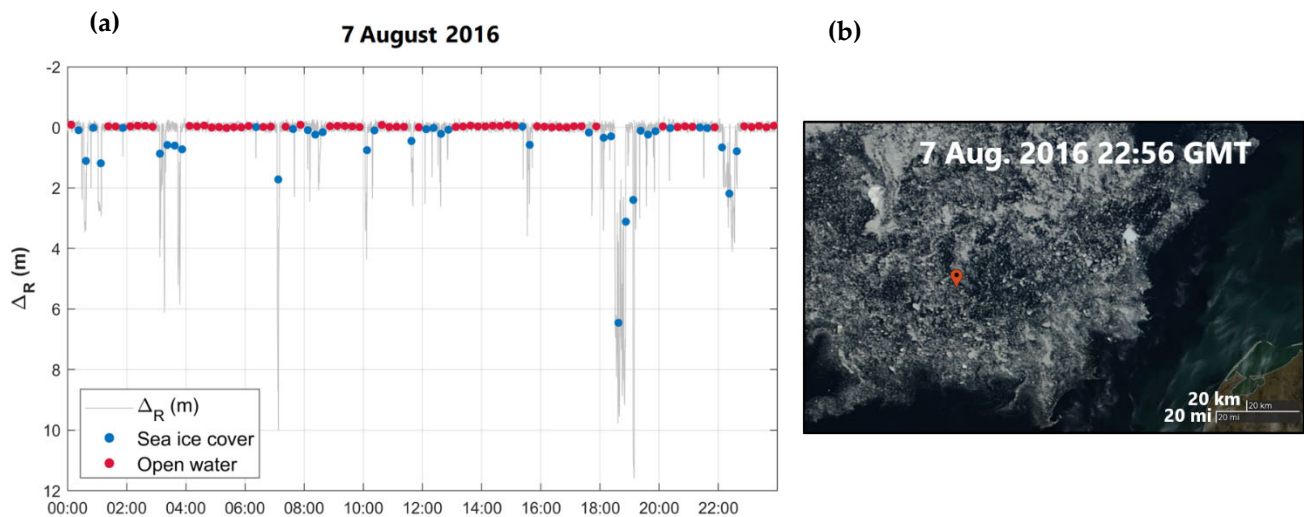

Figure 10. Plot of Δ_R with the SOM analysis for 7 August 2016 with accompanying mostly cloud-free true color Terra/MODIS satellite image. The full-resolution Δ_R time series ((**a**); 20-s ping interval) from the AZFP in the NE Chukchi Sea is plotted in gray, with each 15-min period Δ_R mean marked as Mode 1 (open water; red) or Mode 2 (ice cover; blue) according to the SOM. The red marker's point in the satellite image (**b**) shows the location of the CEO moorings.

Inspection of the SOM maps for the AZFP data suggests that the transition between open water and sea ice during freeze-up typically happens relatively quickly (on the order of hours to days) in November or December, whereas the break-up transition from ice cover to open water in May to September is often a more drawn-out process, occurring over weeks or months, with many "false break-ups" (as defined by Rolph et al. [49]) occurring before the open-water season is sustained. It is during this break-up transition period that the SOM map appears to have the greatest difficulty in delineating open water and sea ice, with occasional open-water ensembles being unrealistically identified at 1–2 m depth. Some of these instances are consequences of the 15-min averaging, wherein occasional deep keels are present in an ensemble that is primarily composed of open water. Other ambiguously classified open-water ensembles may be due to changes in the acoustic properties of sea ice as it melts, a characteristic that warrants further study. To assess the reliability of the SOM, we apply a threshold approach and assume that any 15-min ensemble of Δ_R greater than 0.5 m is likely to be sea ice, noting that large wind-waves tend to average out close to zero over 15 min of measurements. Such ensembles identified by the SOM as open water make up ~0.29% of the six-year dataset, or about the equivalent of one day's worth of ambiguously classified ensembles per year.

Analysis of the AZFP dataset by the SOM provides insight to the physical conditions of the surface ocean and ice environment over the CEO mooring. For example, examining the SOM BMU for 23 September 2014 shows that, unsurprisingly, all of these ensembles are identified as open water (Figure 11a). In contrast, 3 December 2014 (Figure 11b) is identified by the SOM as entirely ice-covered, with the exception of a single 15-min interval just after 03:00 GMT, at the beginning of the longest of the near-zero Δ_R periods, which we identify as a potential lead. Plotting only Δ_R with the SOM BMU here can result in a confusing picture of a lead persisting for about 75 min, yet with only the first 15-min ensemble identified as open water. However, S_v reveals additional information: the amplitude of S_v gradually decreases after the initial appearance of open water. In this instance, a lead appears over the mooring within the time period covered by the open-water ensemble. The next ensemble is identified as ice-covered. This observation suggests that either the lead was partially covered by thin ice that occupied the side of the lead that was last to pass over the mooring, or that an initially open-water lead may have developed a thin ice covering during that time period. The other two near-zero Δ_R periods (at approximately 18:00 and 21:00 GMT) on 3 December 2014 both include S_v values near 0 dB, indicating that some periods of open water likely occurred, but are too short in duration to be identified by the SOM as open water using the 15-min averaging period. These analyses suggest that due to the contrast in acoustic character of the reflected pings, we are able to distinguish leads with open water from leads with thin ice cover, even though the difference in ice draft might be too small to make this distinction using Δ_R alone.
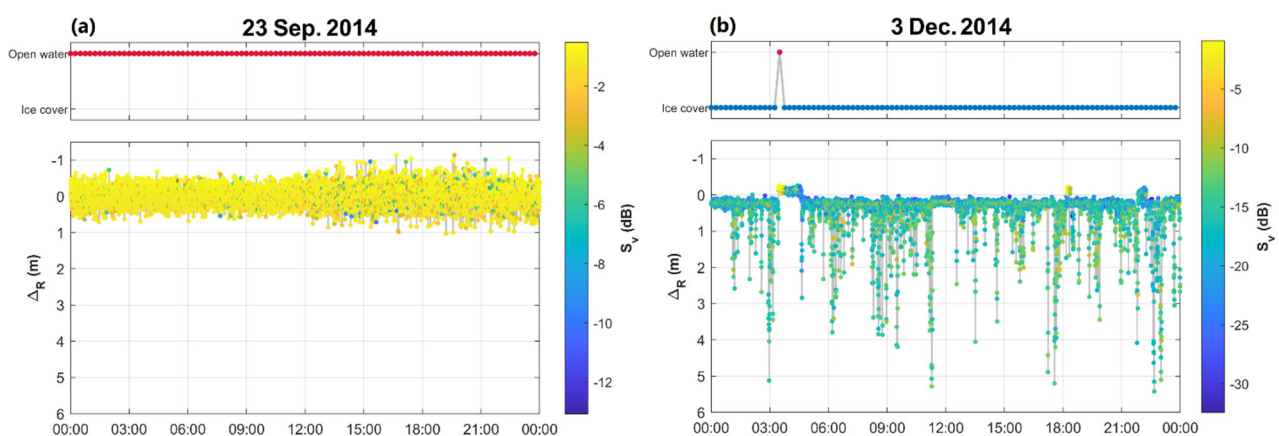

Figure 11. Plots of Δ_R (m) and SOM analysis for representative 24-h intervals, colored by S_v (dB). Δ_R from the AZFP dataset at the CEO site in the NE Chukchi Sea is shown for the open-water interval (**a**), and the ice-covered interval (**b**). Above each plot of Δ_R is the SOM BMU for each ensemble, identifying it as either ice cover (blue) or open water (red).

To independently assess the behavior and fidelity of the SOM we can compare the Δ_R estimates and SOM BMUs with satellite imagery captured over the mooring site. In Figure 12, we find four intervals representing different ice conditions and compare Δ_R for those intervals to true color Terra/MODIS satellite images (NASA Worldview; https://worldview.earthdata.nasa.gov; accessed 4 February 2022).

The image of 15 March 2015 (Figure 12a) shows that the pack ice field surrounding the mooring (the red marker in Figure 12) appears mostly continuous, with few leads apparent in the 250 m resolution satellite image. In this case, no open-water ensembles appear in the SOM BMU. For 27 May 2015 (Figure 12b), the ice field has begun breaking up and consists of many individual floes with open-water leads between them. On this day, several short-duration (i.e., one hour or less) open-water ensembles are identified by the SOM. Finally, on 22 July 2015 (Figure 12c), the CEO is surrounded mostly by open water in the midst of a field of sparse ice floes, which are detected in the SOM. In conjunction with the Δ_R and

BMU time series, these satellite images provide some visual confirmation of the ability for the SOM algorithm to classify sea ice and open-water features within the AZFP dataset.

Over 1–4 June 2017 (Figure 13) the CEO site is near the edge of the pack ice and the SOM indicates an incursion of sea ice for approximately two days; the satellite record reveals the presence of a large ice floe that drifts over the mooring early on 2 June. The large floe is preceded by smaller floes on 1 June, which is reflected both in the SOM BMU and the satellite image. The large floe then drifts away from the CEO late on 3 June, leaving purely open-water conditions at the CEO site on 4 June.

A potential application following separation of open-water ensembles from ice-covered ensembles is the statistical characterization of thermodynamically grown ice and ice thickened mechanically due to rafting and ridging. The SOM can be used to separate out open-water ensembles, which allows us to calculate draft statistics for only the ice-covered ensembles. Krishfield et al. [31] demonstrated a method for tracking changes in categories of ice (e.g., new ice, first-year ice, or rafted/ridged ice) based on modal ice thickness estimates over 10-day means. Fukamachi et al. [18] found that calculating the statistical draft values for 5-day intervals revealed two modes, the larger of which continuously increased throughout the winter season and represented the growth of level ice. The potential of using this dataset to track changes in the undeformed ice thickness above the mooring site can be demonstrated by examining time series of Δ_R estimates for three days approximately one month apart during the winter season of the 2014–2015 deployment: 3 December 2014 (Figure 14a), 5 January 2015 (Figure 14b), and 14 February 2015 (Figure 14c). Histograms of the Δ_R estimates for each day show modal peaks that correspond to the level ice for that day, and which progressively thickens through the time series and the course of the winter.
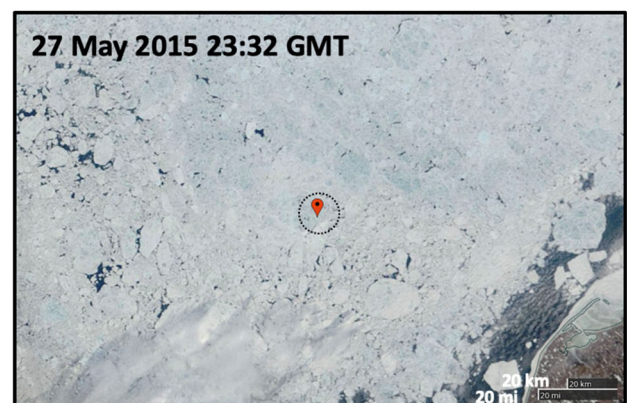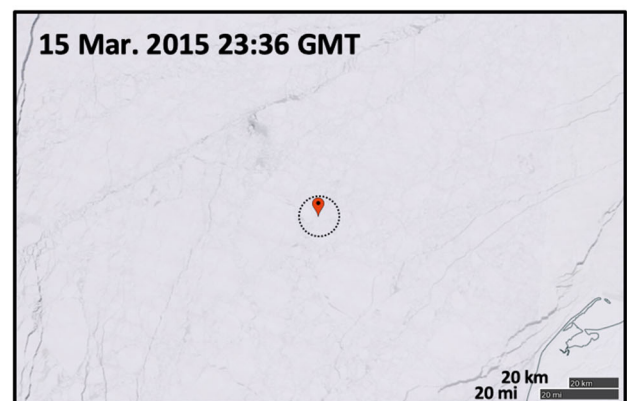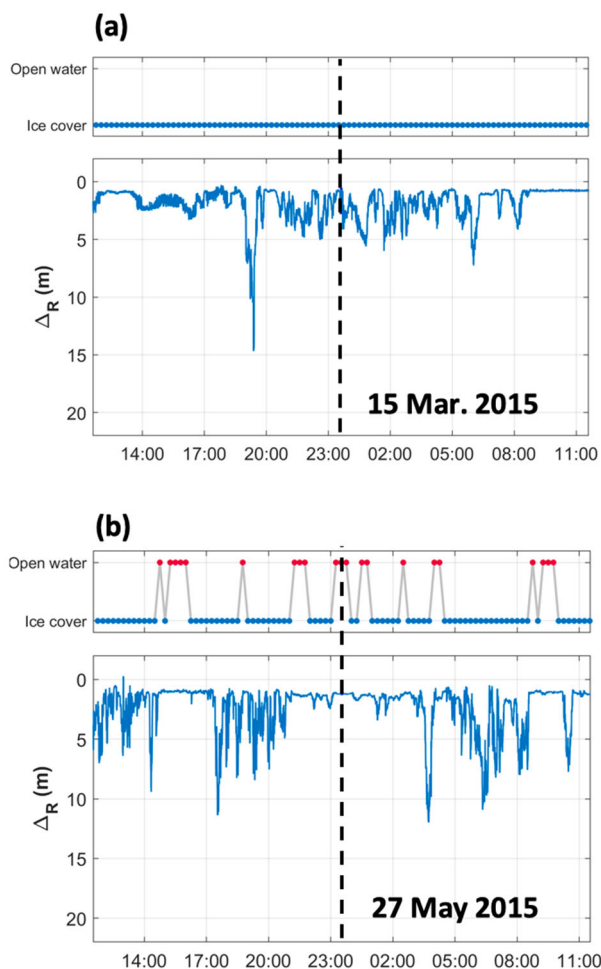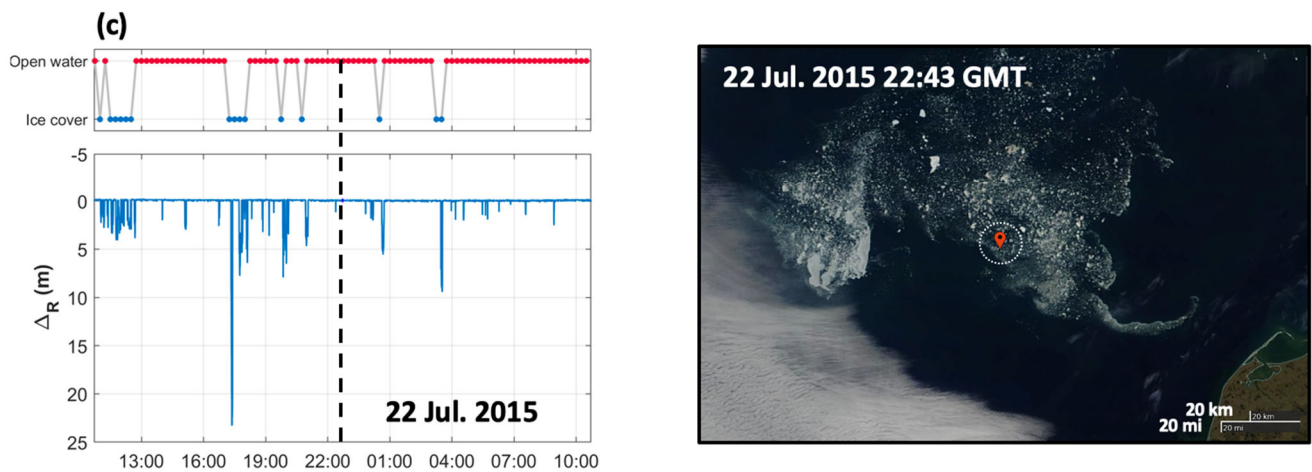

Figure 12. *Cont.*

Figure 12. Examples of Δ_R (m) with corresponding SOM BMUs and accompanying mostly cloud-free true color Terra/MODIS satellite images. Three days from 2015 are plotted for the CEO site in the NE Chukchi Sea: 15 March 2015 (**a**), 27 May 2015 (**b**), and 22 July 2015 (**c**), with Δ_R time series and SOM BMU for each day (left panels; red = open water, blue = ice cover), and satellite images taken in the same day (right panels). The red marker's point in the satellite images shows the location of the CEO moorings. The dashed vertical line in the left panels shows the approximate time of day that the satellite images were acquired, and the dashed circles in the right panels show the approximate distance ice would drift from the mooring site in a 24-h period while moving at a speed of 0.10 m s^{-1}.
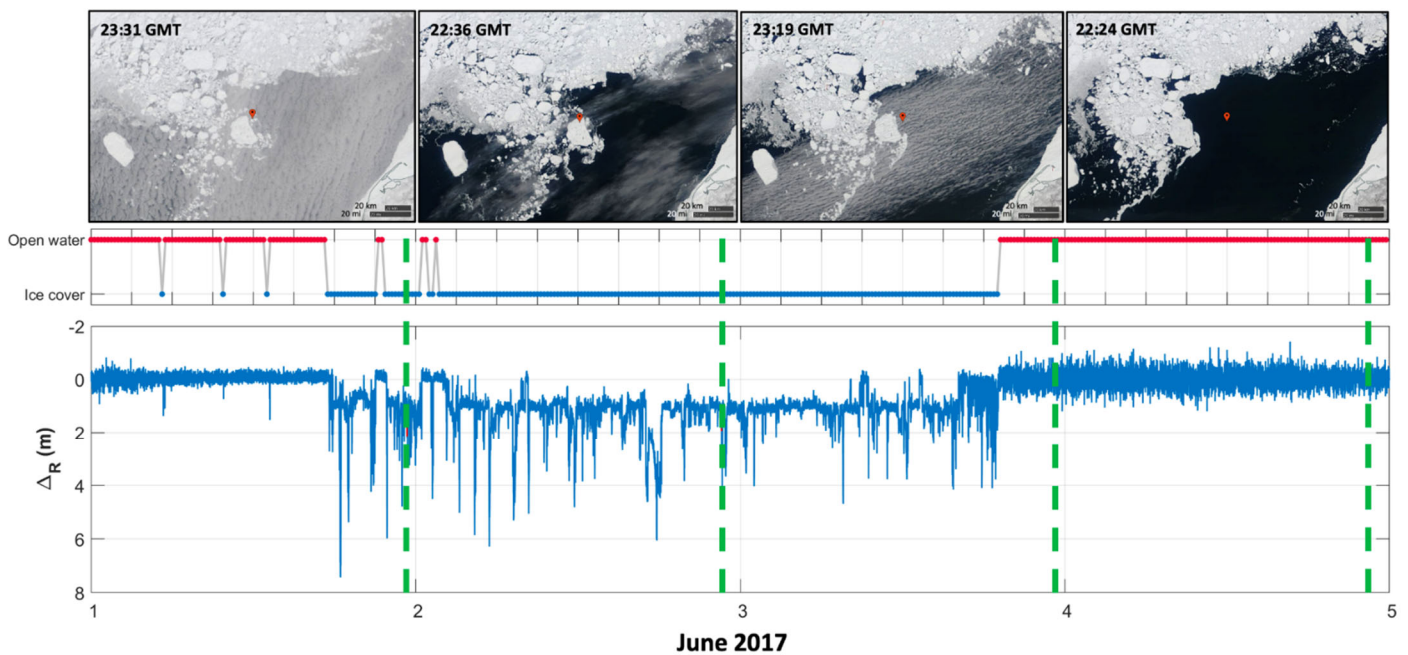

Figure 13. Time series documenting the passage of a large ice floe over the CEO mooring on 1–4 June 2017. The lower panel shows the Δ_R estimates for the four days, the middle panel contains the SOM BMU for the same timeframe, and the upper panels show one true color Terra/MODIS satellite images for each day. The red marker in the satellite images shows the location of the CEO site in the NE Chukchi Sea, and the dashed green line shows the approximate time of each day in which the images were captured.
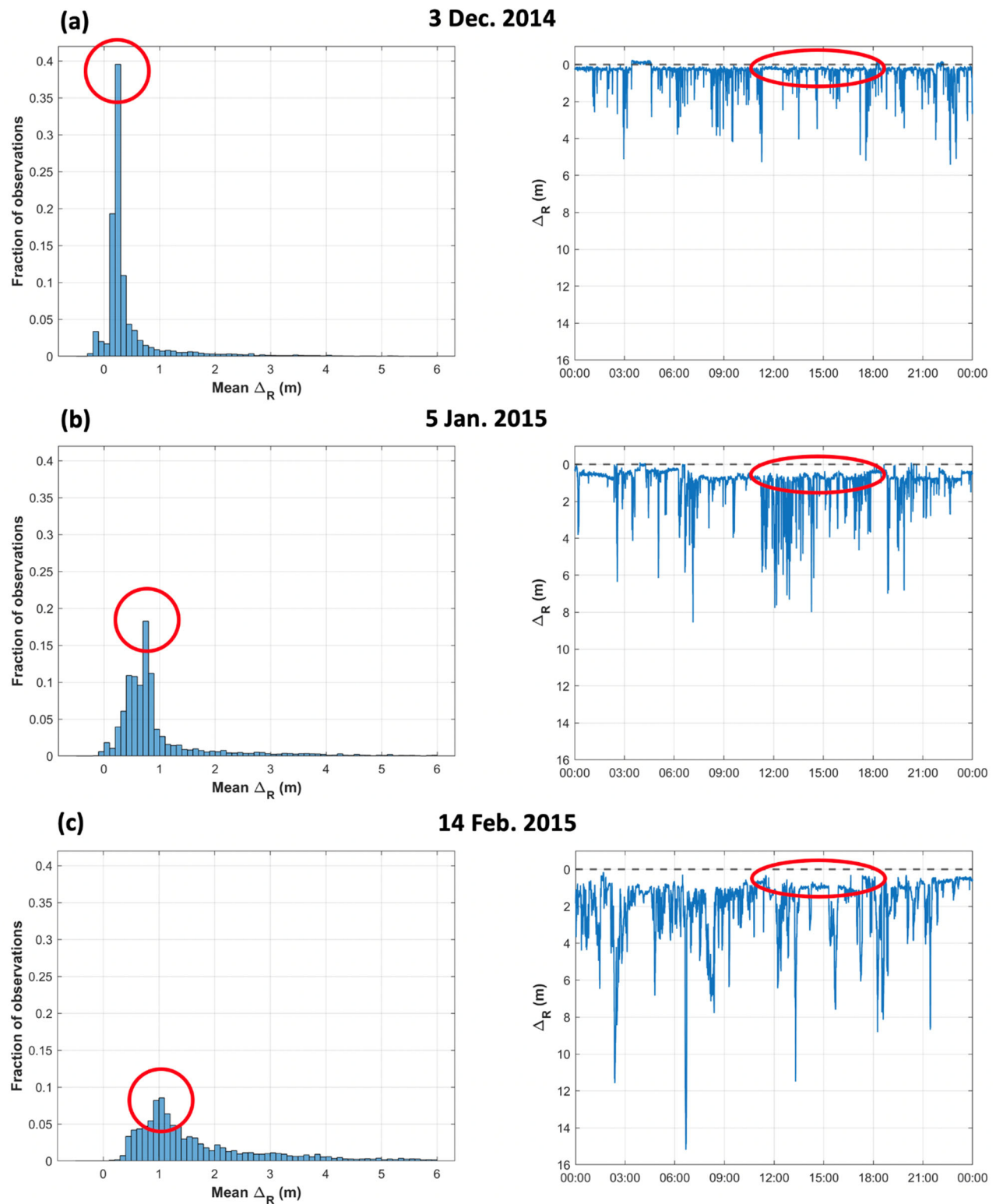
Figure 14. Time series and histograms of Δ_R illustrating changes in level ice thickness. Histograms of Δ_R estimates (10 cm bins) from the AZFP at the CEO site in the NE Chukchi Sea are plotted for 3 December 2014 (**a**), 5 January 2015 (**b**), and 14 February 2015 (**c**), including only pings in which sea ice was present above the CEO mooring (left panels). Corresponding time series of Δ_R are plotted in the right panels. The mode of the Δ_R estimates, circled in red in the histograms, corresponds to the level ice in the Δ_R time series (a representative sample is also circled in red). The dashed black line represents the undisturbed sea level.

3.4. The Surface Wave Field

The identification of open-water time periods and the Δ_R range statistic provides an opportunity to assess the local wave conditions. The 15-min ensemble Δ_R range calculation (the range of Δ_R, measured in m, is simply the difference between the largest and smallest Δ_R values over the course of a 15-min ensemble) shows a close relationship with the significant wave height measurement made by the CEO ADCP (Figure 15). Selecting the Δ_R range ensemble that occurs nearest to each 4-hourly ADCP measurement, we show (Figure 15b) that that AZFP slightly underestimates the ADCP-derived significant wave height but that the two are strongly correlated ($r = 0.89$, $p < 0.001$). This result shows that the AZFP is also capable of quantifying the wave height envelopes, and at a much higher sample rate than the ADCP. The CEO ADCP typically has only enough battery power to make one wave measurement ensemble every four hours through the course of the year. On the other hand, the ADCP measures the directional wave spectra, which contains considerable information that the AZFP does not capture, so the AZFP data is not a replacement for all ADCP-derived wave measurements.

Although similar, the two records do not represent identical parameters: the ADCP-derived significant wave height [50] employs a spectral approach that reports (in our example here) the dominant wave amplitude, while the AZFP record provides a measure of the entire wave field's amplitude envelope. A combined statistical approach and spectral analysis of the Δ_R range could produce an AZFP-derived estimate of the significant wave height, though that is beyond the scope of this study. In some applications, the total wave field amplitude may be even more useful than the significant wave height (e.g., [51,52]).

The AZFP dataset may be sufficient to replace a portion of the ADCP waves functionality if mooring design or cost prohibits the installation of a waves-equipped ADCP, or to supplement ADCP measurements as a backup in the event of instrument failure. Analysis of the measured wave properties is beyond the scope of this study, but we note that the AZFP record should allow us to track changes in the spectral character of low-frequency surface waves (e.g., waves with periods of 40 s and longer) that the CTD pressure record does not resolve. The CTD can resolve only waves having periods of two hours and longer.
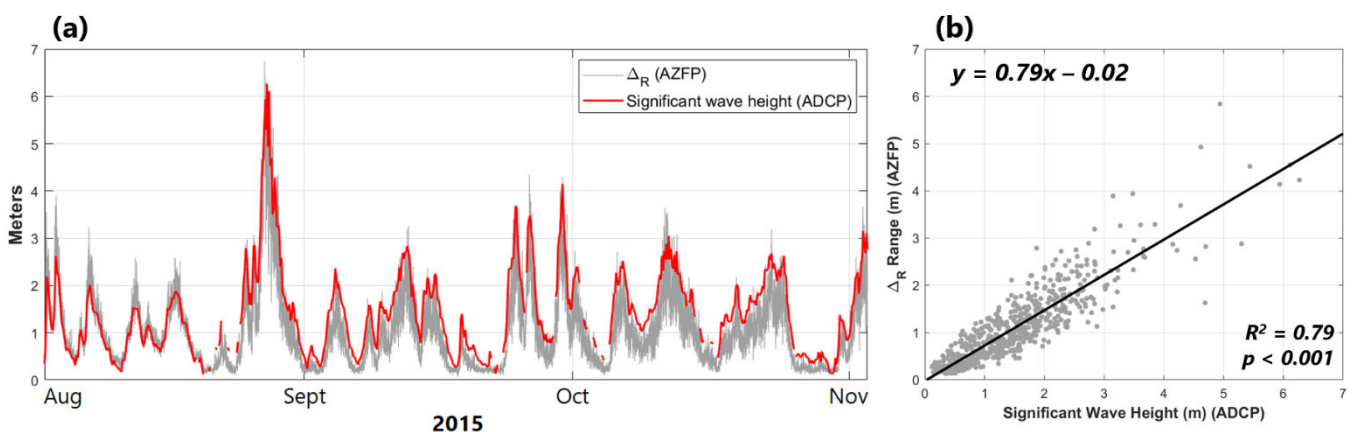

Figure 15. Time series (**a**) and scatter plot (**b**) of significant wave height and range of Δ_R for three months of the open-water season of 2015. Significant wave height was recorded by the ADCP installed on the one of the CEO moorings in the NE Chukchi Sea (in red), and range of Δ_R (15-min ensembles, in gray) is calculated from the AZFP, also from the CEO. The black line in (**b**) represents the least-squares best fit line; with accompanying correlation statistics are noted on the panel.

4. Discussion

Time series of Δ_R estimates allow for the calculation of metrics and statistics for sea ice draft and wave amplitudes, depending on research needs. The high sampling rate of the AZFP allows for the resolution of ice features and open-water events that pass over the

CEO on the scale of minutes to hours. Thus, we can use this dataset to identify, for example, the fraction of an hour in which leads in the sea ice are present above the mooring. This can be used with coincident measurements of ice velocity to calculate sea ice concentration, or as a stand-alone metric that speaks to the temporally changing character of the sea ice field, or the frequency of the occurrence of sparse ice at the CEO site. While an isolated measure of lead recurrence may not be useful in itself, from an ecosystem and environmental monitoring point of view, over time such metrics can provide a means to assess stability or variability in the system. If the instruments detect changes in the recurrence of leads, we may then ask about the importance of such features for brine production, for under-ice phytoplankton blooms, and other physical and ecosystem processes that may be influenced by the presence of leads.

In addition to averaging across modestly fine temporal scales (e.g., minutes), we can also combine the dataset into coarser-scale (e.g., daily) statistical summaries, which would be appropriate for bundling data at the same time scale as passive microwave satellite and OISST records, or at the time scales often used in the analyses of passive acoustic data. Utilizing the SOM BMUs, we can, for example, calculate the fraction of a given time period that contains open water, ice cover, sparse ice flows, ice of any particular draft, waves of any particular height, or spectral wave content. Such metrics can contribute to a more complete picture of ecosystem conditions at the CEO site and can be used to help evaluate the results from numerical models, which often lack in situ data suitable for robust data-model comparisons in the Arctic.

Rates of surface heat fluxes between the ocean to the atmosphere, ice production, and brine rejection are all affected by the presence of leads in the sea ice [53,54]. However, these rates are strongly dependent on the fraction of open water, the processes of refreezing leads, and the presence of young, thin ice [55,56]. Therefore, being able to accurately identify periods and dimensions of open water, thin ice, and thick ice will enable more precise estimation of ocean–atmosphere heat transfers in the ice-covered months, and impacts of ice formation on water column mixing and dense bottom water formation [53]. These estimates can contribute to informing local energy budgets and further updating and evaluating oceanographic and climate models.

While Δ_R produces a measurement of the sea ice draft or wave height at the time of detection of the return echo, it does not provide meaningful spatial information beyond the mooring site. Data on the velocity of sea ice, for example, combined with ULS draft measurements, can be used to estimate the shapes of under-ice features, or the extent of a lead passing over the mooring. A complete analysis of the ice and wave environment at a site such as the CEO should incorporate velocity data from sources such as an ADCP or satellite products. Mahoney et al. [57] performed a comparison of ADCP- and satellite-based ice velocity data in a study of changes in ice thickness distributions in the Beaufort Gyre and found that the resulting distributions were similar.

Our AZFP sampling setup is based on battery capacity limitations that impose limits on resolvable features. The temporal resolution of 10–20 s per ping used in this study aliases the shape of under-ice structures in the presence of typical ice drift speeds. Generally, ULS instruments deployed for ice tracking sample at a rate of 1 Hz [27], and thus can resolve features having 1-m length scales in the presence of typical ocean currents (e.g., $0.10\ \mathrm{m\ s^{-1}}$). For the typical current speed at 10 m depth of about $0.10\ \mathrm{m\ s^{-1}}$ at the CEO site (the 2014–2015 CEO ADCP measured median, mode, and mean speeds of $0.10\ \mathrm{m\ s^{-1}}$, $0.06\ \mathrm{m\ s^{-1}}$, and $0.12\ \mathrm{m\ s^{-1}}$, respectively) and assuming similar ice speed (e.g., see [58,59]), a 15-s ping rate can only identify features (e.g., ice keels or leads) with a Nyquist length scale larger than 3 m. However, even these relatively small features will be obscured by 15-min averaging. For the $0.10\ \mathrm{m\ s^{-1}}$ current speed, the 15-min-averaged period is capable of identifying features with horizontal length scales only larger than 180 m. For an upper bound current speed of $1\ \mathrm{m\ s^{-1}}$ (the maximum observed speed in the 2014–2015 CEO deployment was less than $0.60\ \mathrm{m\ s^{-1}}$), the smallest resolvable length scale extends to 1.8 km.

Caution should be exercised in statistical analyses and interpretation of Δ_R based on ensemble averages. As previously stated, the 15-min ensembles may contain a combination of open-water and ice-covered pings regardless of how the ensemble is ultimately classified by the SOM. Thus, features that are smaller in scale than the averaging period may be aliased. In addition, the ensemble averaging can have an effect on the distribution of the Δ_R values due to the nonlinear nature of ice keel probability distributions. For example, while the mean Δ_R of the six-year full-resolution dataset barely varies (a difference of ~1 cm) between15-min, hourly, and daily ensembles, the modes vary by up to 8 cm, and the medians as much as 21 cm. Hence, the ensemble length selection introduces biases that could be important for some applications.

Another inherent limitation of an AZFP installed on a subsurface mooring is that it lacks wider environmental context. In the case of the CEO, ascertaining the influence of the Hanna Shoal topography on the ice environment at the mooring site and how this compares to conditions elsewhere on the Chukchi Sea shelf is important for a variety of research needs, such as our ability to understand the variability of rapidly changing habitats for species that depend on sea ice cover that is responding to climate change. To answer this question, the automated processing procedure we have developed here can be applied to additional ULS datasets.

The effectiveness of the SOM is modestly dependent on the input variables that are provided to the algorithm. Histograms of each of the statistics used in this study (Figure 16) illustrate how each of these contrast in open-water and ice-covered conditions. For most Δ_R histograms, the peaks for open-water and ice-covered ensembles are often in the same range of values, but the character of the curves contrast. Distributions for the ice-covered ensembles tend to be skewed toward the positive direction and represent a wider range of Δ_R values, as they include ice keels, whereas the open-water curves tend to be more symmetrical (consistent with waves oscillating about undisturbed sea level) with a shorter range of Δ_R values and sharper peaks. In most cases, the histograms of S_v exhibit peaks at different ranges of S_v for open water than for ice cover, though the character of the curves varies. All together, these histograms further illustrate how we can take advantage of these differences to distinguish open water from ice cover, and why these variables are appropriate for use in the SOM algorithm.

A number of future steps could further improve the algorithm that produces Δ_R. For instance, the configuration of our AZFP offers opportunities to gather more information by investigating the acoustic returns of three additional frequencies. We can also continue to explore the functionality of the SOM algorithm; for example, the SOM could be configured to sort the Δ_R ensembles into three or more modes to extract additional facets of the ice environment. More research is needed to understand the characteristics of ablating sea ice that produces anomalous open-water ensembles during break-up periods at the CEO site. Ground-truthing the acoustic determinations using an alternate sea ice identification approach (e.g., camera or direct visual observation) is needed to more fully assess the accuracy of the SOM BMU assignments.
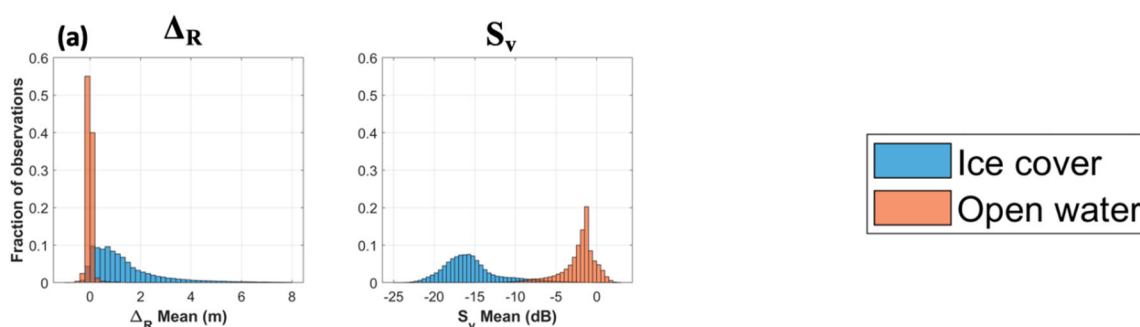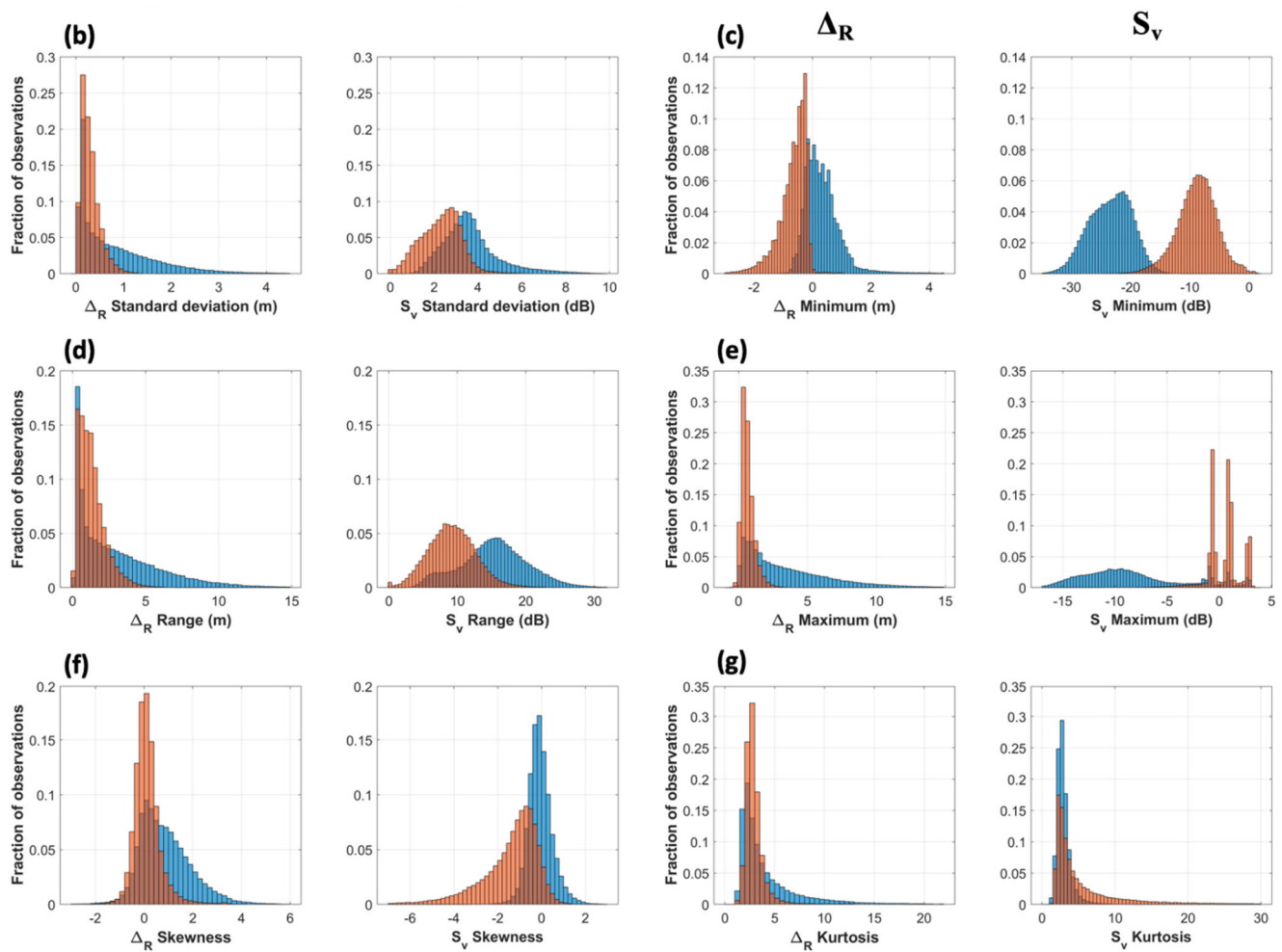

Figure 16. *Cont.*

Figure 16. Histograms for each of the statistics provided to the SOM for the six-year AZFP dataset. The statistics used are: mean (**a**), standard deviation (**b**), range (**d**), skewness (**f**), kurtosis (**g**), minimum (**c**), and maximum (**e**) for both Δ_R (left panel of each pair) and S_v (right panel of each pair). Ensembles identified by the SOM as open water for the CEO site in the NE Chukchi Sea are plotted in orange, and those identified as ice cover are plotted in blue. Note the different axes for each variable pair.

5. Conclusions

The subsurface oceanographic moorings of the CEO site enable physical, chemical, and biological sampling of the water column all year long, allowing us to build a more complete understanding of the seasonal environmental variations near Hanna Shoal. The AZFP, a ULS installed on one of the CEO moorings, provides a high-resolution dataset from which we can extract information that helps us characterize the sea ice and surface wave environment at the CEO site.

We developed a method for calculating a time series of Δ_R, the distance between the local undisturbed sea level and the ocean–ice or ocean–atmosphere interface. Corrections for instrument tilt, speed of sound, and water level allow us to resolve the sea surface reflection interface to within approximately 0.06 ± 0.09 m (mean and standard error).

As the processing of high-resolution acoustic datasets for evaluating ice draft has traditionally been a labor-intensive process, we applied a machine-learning technique to leverage acoustic differences between the ocean-sea ice and the ocean–atmosphere interfaces for identifying which pings from the AZFP pings occurred under open water or sea ice cover. The approach is more efficient than the often manual procedures employed by previous studies. The procedure allows us to implement automated corrections of Δ_R for periods of ice cover when the ocean–atmosphere interface is obscured.

With the resulting dataset, we are able to detect short-duration features such as the frequency of sparse ice floes, leads, and sea ice draft. When combined with ice velocity data from other sources, this also allows for the construction of lead width and ice volume advection estimates at the CEO site. We can compute metrics such as the fraction of time in a given period that contains ice leads, or the frequency of occurrence for ice keels of a particular draft. With AZFP estimates of wave height, we can quantify temporal changes in the wave field over the mooring. All together, the applications of this high-resolution acoustic dataset enable a richer characterization of the biologically important physical environment at the mooring site, and the algorithms developed facilitate the efficient processing of ULS data from existing and future mooring deployments.

References

1. Pachauri, R.K.; Allen, M.R.; Barros, V.R.; Broome, J.; Cramer, W.; Christ, R.; Church, J.A.; Clarke, L.; Dahe, Q.; Dasgupta, P.; et al. *Climate Change 2014: Synthesis Report*; Contribution of Working Groups I, II and III to the Fifth Assessment Report of the Intergovernmental Panel on Climate Change/R; Pachauri, R.K., Meyer, L., Eds.; IPCC: Geneva, Switzerland, 2014; 151p, ISBN 978-92-9169-143-2.
2. Woodgate, R.A.; Weingartner, T.; Lindsay, R. The 2007 Bering Strait oceanic heat flux and anomalous Arctic sea-ice retreat. *Geophys. Res. Lett.* **2010**, *37*, L01602. [CrossRef]
3. Carmack, E.C.; Yamamoto-Kawai, M.; Haine, T.W.; Bacon, S.; Bluhm, B.A.; Lique, C.; Melling, H.; Polyakov, I.V.; Straneo, F.; Timmermans, M.L.; et al. Freshwater and its role in the Arctic Marine System: Sources, disposition, storage, export, and physical and biogeochemical consequences in the Arctic and global oceans. *J. Geophys. Res. Biogeosci.* **2016**, *121*, 675–717. [CrossRef]
4. Meier, W.N.; Hovelsrud, G.K.; Van Oort, B.E.H.; Key, J.R.; Kovacs, K.M.; Michel, C.; Haas, C.; Granskog, M.A.; Gerland, S.; Perovich, D.K.; et al. Arctic sea ice in transformation: A review of recent observed changes and impacts on biology and human activity. *Rev. Geophys.* **2014**, *51*, 185–217. [CrossRef]
5. Stroeve, J.C.; Serreze, M.C.; Holland, M.M.; Kay, J.E.; Malanik, J.; Barrett, A.P. The Arctic's rapidly shrinking sea ice cover: A research synthesis. *Clim. Chang.* **2012**, *110*, 1005–1027. [CrossRef]
6. Grebmeier, J.M.; Cooper, L.W.; Feder, H.M.; Sirenko, B.I. Ecosystem dynamics of the Pacific-influenced Northern Bering and Chukchi Seas in the Amerasian Arctic. *Prog. Oceanogr.* **2006**, *71*, 331–361. [CrossRef]
7. Danielson, S.L.; Ahkinga, O.; Ashjian, C.; Basyuk, E.; Cooper, L.W.; Eisner, L.; Farley, E.; Iken, K.B.; Grebmeier, J.M.; Juranek, L.; et al. Manifestation and consequences of warming and altered heat fluxes over the Bering and Chukchi Sea continental shelves. *Deep-Sea Res. Part II Top. Stud. Oceanogr.* **2020**, *177*, 104781. [CrossRef]
8. Woodgate, R.A.; Aagaard, K.; Weingartner, T.J. A year in the physical oceanography of the Chukchi Sea: Moored measurements from autumn 1990–1991. *Deep-Sea Res. Part II Top. Stud. Oceanogr.* **2005**, *52*, 3116–3149. [CrossRef]

9. Lu, K.; Danielson, S.; Hedstrom, K.; Weingartner, T. Assessing the role of oceanic heat fluxes on ice ablation of the central Chukchi Sea shelf. *Prog. Oceanogr.* **2020**, *184*, 102313. [CrossRef]
10. Fang, Y.C.; Weingartner, T.J.; Dobbins, E.L.; Winsor, P.; Statscewich, H.; Potter, R.A.; Mudge, T.D.; Stoudt, C.A.; Borg, K. Circulation and thermohaline variability of the Hanna Shoal region on the northeastern Chukchi Sea shelf. *J. Geophys. Res. Oceans* **2020**, *125*, e2019JC015639. [CrossRef]
11. Carmack, E.; Wassmann, P. Food webs and physical-biological coupling on pan-Arctic shelves: Unifying concepts and comprehensive perspectives. *Prog. Oceanogr.* **2006**, *71*, 446–477. [CrossRef]
12. Weingartner, T.; Aagaard, K.; Woodgate, R.; Danielson, S.; Sasaki, Y.; Cavalieri, D. Circulation on the north central Chukchi Sea shelf. *Deep-Sea Res. Part II Top. Stud. Oceanogr.* **2005**, *52*, 3150–3174. [CrossRef]
13. Walsh, J.J.; McRoy, C.P.; Coachman, L.K.; Goering, J.J.; Nihoul, J.J.; Whitledge, T.E.; Blackburn, T.H.; Parker, P.L.; Wirick, C.D.; Shuert, P.G.; et al. Carbon and nitrogen cycling within the Bering/Chukchi Seas: Source regions for organic matter effecting AOU demands of the Arctic Ocean. *Prog. Oceanogr.* **1989**, *22*, 277–359. [CrossRef]
14. Hennon, T.D.; Danielson, S.L.; Woodgate, R.; Irving, B.; Stockwell, D.; Mordy, C. Mooring measurements of Anadyr Current nitrate, phosphate, and silicate enable updated Bering Strait nutrient flux estimates. *Geophys. Res. Lett.* **2022**, *49*, e2022GL098908. [CrossRef]
15. Grebmeier, J.M.; McRoy, C.P.; Feder, H.M. Pelagic-benthic coupling on the shelf of the northern Bering and Chukchi Seas. I. Food supply source and benthic biomass. *Mar. Ecol. Prog. Ser.* **1988**, *48*, 57–67. [CrossRef]
16. Codispoti, L.A.; Flagg, C.; Kelly, V.; Swift, J.H. Hydrographic conditions during the 2002 SBI process experiments. *Deep-Sea Res. Part II Top. Stud. Oceanogr.* **2005**, *52*, 3199–3226. [CrossRef]
17. Mahoney, A.R.; Eicken, H.; Fukamachi, Y.; Ohshima, K.I.; Simizu, D.; Kambhamettu, C.; Rohith, M.V.; Hendricks, S.; Jones, J. Taking a look at both sides of the ice: Comparison of ice thickness and drift speed as observed from moored, airborne and shore-based instruments near Barrow. *Alaska Ann. Glaciol.* **2015**, *56*, 363–372. [CrossRef]
18. Fukamachi, Y.; Simizu, D.; Ohshima, K.I.; Eicken, H.; Mahoney, A.R.; Iwamoto, K.; Moriya, E.; Nihashi, S. Sea-ice thickness in the coastal northeastern Chukchi Sea from moored ice-profiling sonar. *J. Glaciol.* **2017**, *63*, 888–898. [CrossRef]
19. Barrett, S.A.; Stringer, W.J. Growth Mechanisms of "Katie's Floeberg". *Arct. Alp. Res.* **1978**, *10*, 775–783. [CrossRef]
20. Grebmeier, J.M.; Bluhm, B.A.; Cooper, L.W.; Danielson, S.L.; Arrigo, K.R.; Blanchard, A.L.; Clarke, J.T.; Day, R.H.; Frey, K.E.; Gradinger, R.R.; et al. Ecosystem characteristics and processes facilitating persistent microbenthic biomass hotspots and associated benthivory in the Pacific Arctic. *Prog. Oceanogr.* **2015**, *136*, 92–114. [CrossRef]
21. Jay, C.V.; Fischbach, A.S.; Kochnev, A.A. Walrus areas of use in the Chukchi Sea during sparse sea ice cover. *Mar. Ecol. Prog. Ser.* **2012**, *468*, 1–13. [CrossRef]
22. Iken, K.; Mueter, F.; Grebmeier, J.M.; Cooper, L.W.; Danielson, S.L.; Bluhm, B.A. Developing an observational design for epibenthos and fish assemblages in the Chukchi Sea. *Deep-Sea Res. Part II Top. Stud. Oceanogr.* **2019**, *162*, 180–190. [CrossRef]
23. Danielson, S.L.; Iken, K.; Hauri, C.; Hopcroft, R.R.; McDonnell, A.M.P.; Winsor, P.; Lalande, C.; Grebmeier, J.M.; Cooper, L.W.; Horne, J.K.; et al. Collaborative approaches to multi-disciplinary monitoring of the Chukchi shelf marine ecosystem: Networks of networks for maintaining long-term Arctic observations. In Proceedings of the Oceans 2017—Anchorage, Anchorage, AK, USA, 18–21 September 2017.
24. Hauri, C.; Danielson, S.; McDonnell, A.M.P.; Hopcroft, R.R.; Winsor, P.; Shipton, P.; Lalande, C.; Stafford, K.M.; Horne, J.K.; Cooper, L.W.; et al. From sea ice to seals: A moored marine ecosystem observatory in the Arctic. *Ocean Sci.* **2018**, *14*, 1423–1433. [CrossRef]
25. McCammon, M. *Arctic Build-Out Plan 2013, Alaska Ocean Observing System*; Alaska Ocean Observing System: Anchorage, AK, USA, 2013; 8p.
26. Lalande, C.; Grebmeier, J.M.; Hopcroft, R.R.; Danielson, S.L. Annual cycle of export fluxes of biogenic matter near Hanna Shoal in the northeast Chukchi Sea. *Deep-Sea Res. Part II Top. Stud. Oceanogr.* **2020**, *177*, 104730. [CrossRef]
27. Birch, R.; Fissel, D.; Melling, H.; Vaudrey, K.; Lamb, W.; Schaudt, K.; Heideman, J. Ice-profiling sonar. *Sea Technol.* **2000**, *41*, 48–54.
28. Melling, H.; Johnston, P.H.; Riedel, D.A. Measurements of the underside topography of sea ice by moored subsea sonar. *J. Atmos. Ocean. Technol.* **1995**, *12*, 589–602. [CrossRef]
29. Strass, V.H. Measuring sea ice draft and coverage with moored upward looking sonars. *Deep-Sea Res. Part I* **1998**, *45*, 795–818. [CrossRef]
30. Kvambekk, Å.S.; Vinje, T. *Ice Draft Recordings from Upward Looking Sonars (ULSs) in the Fram Strait and the Barents Sea in 1987/88 and 1990/91*; Norsk Polarinstitutt Rapportse; Norwegian Polar Research Institute: Oslo, Norway, 1992; Volume 79.
31. Krishfield, R.A.; Proshutinsky, A.; Tateyama, K.; Williams, W.J.; Carmack, E.C.; McLaughlin, F.A.; Timmermans, M.-L. Deterioration of perennial sea ice in the Beaufort Gyre from 2003 to 2012 and its impact on the oceanic freshwater cycle. *J. Geophys. Res. Oceans* **2014**, *119*, 1271–1305. [CrossRef]
32. Melling, H. Sound scattering from sea ice: Aspects relevant to ice-draft profiling by sonar. *J. Atmos. Ocean Technol.* **1998**, *15*, 1023–1034. [CrossRef]
33. Jezek, K.C.; Stanton, T.K.; Gow, A.J.; Lange, M.A. Influence of environmental conditions on acoustical properties of sea ice. *J. Acoust. Soc.* **1990**, *88*, 1903–1912. [CrossRef]
34. Light, B.; Maykut, G.A.; Grenfell, T.C. Effects of temperature on the microstructure of first-year Arctic sea ice. *J. Geophys. Res.* **2003**, *108*, 3051. [CrossRef]

35. Onana, V.; Kurtz, N.T.; Farrell, S.L.; Koenig, L.S.; Studinger, M.; Harbeck, J.P. A sea-ice lead detection algorithm for use with high-resolution airborne visible imagery. *IEEE Trans. Geosci. Remote Sens.* **2013**, *51*, 38–56. [CrossRef]

36. Hutter, N.; Zampieri, L.; Losch, M. Leads and ridges in Arctic sea ice from RGPS data and a new tracking algorithm. *Cryosphere* **2019**, *13*, 627–645. [CrossRef]

37. Behrendt, A.; Dierking, W.; Fahrbach, E.; Witte, H. Sea ice draft in the Weddell Sea, measured by upward looking sonars. *Earth Syst. Sci. Data* **2013**, *5*, 209–226. [CrossRef]

38. Gonzalez, S.; Horne, J.K.; Danielson, S.L. Multi-scale temporal variability in biological-physical associations in the NE Chukchi Sea. *Polar Biol.* **2021**, *44*, 837–855. [CrossRef]

39. Skyllingstad, E.D.; Paulson, C.A.; Pegau, W.S.; McPhee, M.G.; Stanton, T. Effects of keels on ice bottom turbulence exchange. *J. Geophys. Res.* **2003**, *108*, 3372. [CrossRef]

40. Pawlowicz, R.; Beardsley, B.; Lentz, S. Classical tidal harmonic analysis including error estimates in MATLAB using T_TIDE. *Comput. Geosci.* **2002**, *28*, 929–937. [CrossRef]

41. Kohonen, T. The self-organizing map. *Neurocomputing* **1998**, *21*, 1–6. [CrossRef]

42. Richardson, A.J.; Risien, C.; Shillington, F.A. Using self-organizing maps to identify patterns in satellite imagery. *Prog. Oceanogr.* **2003**, *59*, 223–239. [CrossRef]

43. Liu, Y.; Weisberg, R.H.; Mooers, C.N.K. Performance evaluation of the self-organizing map for feature extraction. *J. Geophys. Res.* **2006**, *3*, C05018. [CrossRef]

44. Mihanović, H.; Cosoli, S.; Vilibić, I.; Ivanković, D.; Dadić, V.; Gačić, M. Surface current patterns in the northern Adriatic extracted from high-frequency radar data using self-organizing map analysis. *J. Geophys. Res.* **2011**, *116*, C08033. [CrossRef]

45. Kohonen, T. Self-organized formation of topologically correct feature maps. *Biol. Cybern.* **1982**, *43*, 59–69. [CrossRef]

46. Maslanik, J.; Stroeve, J. *Near-Real-Time DMSP SSMIS Daily Polar Gridded Sea Ice Concentrations, Version 1*; electronic dataset; NASA National Snow and Ice Data Center Distributed Active Archive Center: Boulder, CO, USA, 1999.

47. Gloersen, P. *Nimbus-7 SMMR Polar Gridded Radiances and Sea Ice Concentrations, Version 1*; electronic dataset; NASA National Snow and Ice Data Center Distributed Active Archive Center: Boulder, CO, USA, 2006.

48. Stanton, T.J.; Jezek, K.C.; Gow, A.J. Acoustical reflection and scattering from the underside of laboratory grown sea ice: Measurements and predictions. *J. Acoust. Soc.* **1986**, *80*, 1486–1494. [CrossRef]

49. Rolph, R.J.; Mahoney, A.R.; Walsh, J.; Loring, P.A. Impacts of a lengthening open water season on Alaskan coastal communities: Deriving locally relevant indices from large-scale datasets and community observations. *Cryosphere* **2018**, *12*, 1779–1790. [CrossRef]

50. Baxevani, A.; Caires, S.; Rychlik, I. Spatio-temporal statistical modelling of significant wave height. *Environmetrics* **2008**, *20*, 14–31. [CrossRef]

51. Felizardo, F.C.; Melville, W.K. Correlations between ambient noise and the ocean surface wave field. *J. Phys. Oceanogr.* **1995**, *25*, 513–532. [CrossRef]

52. Ahn, S. Modeling mean relation between peak period and energy period of ocean surface wave systems. *Ocean Eng.* **2021**, *228*, 108937. [CrossRef]

53. Eisen, O.; Kottmeier, C. On the importance of leads in sea ice to the energy balance and ice formation in the Weddell Sea. *J. Geophys. Res.* **2000**, *105*, 14045–14060. [CrossRef]

54. Lüpkes, C.; Vihma, T.; Birnbaum, G.; Wacker, U. Influence of leads in sea ice on the temperature of the atmospheric boundary layer during polar night. *Geophys. Res. Lett.* **2008**, *35*, L03805. [CrossRef]

55. Stigebrandt, A. A model for the thickness and salinity of the upper layer in the Arctic Ocean and the relationship between the ice thickness and some external parameters. *J. Phys. Oceanogr.* **1981**, *11*, 1407–1422. [CrossRef]

56. Maykut, G.A. Large-scale heat exchange and ice production in the central Arctic. *J. Geophys. Res.* **1982**, *87*, 7971–7984. [CrossRef]

57. Mahoney, A.R.; Hutchings, J.K.; Eicken, H.; Haas, C. Changes in the thickness and circulation of multiyear ice in the Beaufort Gyre determined from pseudo-Lagrangian methods from 2003–2015. *J. Geophys. Res. Oceans* **2019**, *124*, 5618–5633. [CrossRef]

58. Norton, D.W.; Gaylord, A.G. Drift velocities of ice floes in Alaska's northern Chukchi Sea flaw zone: Determinants of success by spring subsistence whalers in 2000 and 2001. *Arctic* **2004**, *57*, 347–362. [CrossRef]

59. Kwok, R.; Spreen, G.; Pang, S. Arctic sea ice circulation and drift speed: Decadal trends and ocean currents. *J. Geophys. Res. Oceans* **2013**, *118*, 2408–2425. [CrossRef]